Modulation of Reactivity and Conformation within the T-Quaternary State of Human Hemoglobin: The Combined Use of Mutagenesis and Sol−Gel Encapsulation[†]

Uri Samuni, Camille J. Roche, David Dantsker, Laura J. Juszczak, and Joel M. Friedman*

Department of Physiology and Biophysics, Albert Einstein College of Medicine, Bronx, New York 10461

Received January 3, 2005; Revised Manuscript Received January 4, 2006

ABSTRACT: A range of conformationally distinct functional states within the T quaternary state of hemoglobin are accessed and probed using a combination of mutagenesis and sol−gel encapsulation that greatly slow or eliminate the T → R transition. Visible and UV resonance Raman spectroscopy are used to probe the proximal strain at the heme and the status of the $\alpha_1\beta_2$ interface, respectively, whereas CO geminate and bimolecular recombination traces in conjunction with MEM (maximum entropy method) analysis of kinetic populations are used to identify functionally distinct T-state populations. The mutants used in this study are Hb(Nβ102A) and the α99-α99 cross-linked derivative of Hb(Wβ37E). The former mutant, which binds oxygen noncooperatively with very low affinity, is used to access low-affinity ligated T-state conformations, whereas the latter mutant is used to access the high-affinity end of the distribution of T-state conformations. A pattern emerges within the T state in which ligand reactivity increases as both the proximal strain and the $\alpha_1\beta_2$ interface interactions are progressively lessened after ligand binding to the deoxy T-state species. The ligation and effector-dependent interplay between the heme environment and the stability of the Trp β37 cluster in the hinge region of the $\alpha_1\beta_2$ interface appears to determine the distribution of the ligated T-state species generated upon ligand binding. A qualitative model is presented, suggesting that different T quaternary structures modulate the stability of different $\alpha\beta$ dimer conformations within the tetramer.

Allosteric transitions represent an important mechanism for regulating protein reactivity. Hemoglobin has been and continues to be the prototype for studying the molecular basis of allostery. For hemoglobin as well as for other allosteric proteins, well-characterized initial and final endpoint structures form the basis for most mechanistic models put forth to account for the observed allostery. The MWC two-state model (*1*), used to explain many of the salient aspects of allostery within the hemoglobin tetramer, was based largely on the premise that there are oxygenation-dependent changes in the equilibrium between two functionally distinct quaternary states: the low-affinity T quaternary state and the high-affinity R quaternary state (*2*−*6*). These states are correlated with the T- and R-quaternary structures derived primarily from X-ray crystallographic studies on two stable endpoint Hb species, deoxyHb and fully ligated Hb, respectively.

A growing number of studies indicate that a detailed molecular understanding of allostery in Hb requires the consideration of more than two affinity states. X-ray crystallographic measurements (*7*) and NMR solution-phase studies (*8*) have shown that fully ligated hemoglobin manifests an ensemble, the R^e ensemble, of energetically similar but spatially distinct quaternary structures. In contrast, several high-resolution crystallographic studies have shown that fully deoxygenated hemoglobin has virtually the same T quaternary structure under high-salt and low-salt crystallization conditions (*9*−*11*). Such a structural observation might reasonably be construed to imply that the T state should have a narrow range of ligand binding properties; however, this is not the case. The ligand binding properties of the T state show considerable variability in response to the presence of effectors (*12*−*19*), partial ligation (*20*, *21*), partial replacement of the four heme irons with other metals (*16*, *18*, *19*, *22*, *23*), and mutations associated with the so-called hinge region of the $\alpha_1\beta_2$ interface (*24*−*26*). Such observations suggest that the T state is capable of manifesting considerably more conformational and functional plasticity than is implied by the crystallographic studies of deoxy HbA.[1]

Thermodynamic studies (*20*, *21*, *24*, *27*) have revealed both a third affinity state and a set of symmetry rules that determine the energy cost of oxygenation for partially ligated intermediates that together imply the existence of low- and high-affinity T states. Oxygen-titration studies on sol−gel-encapsulated hemoglobin have also revealed low- and high-affinity T-state populations (*28*, *29*). More recently, an X-ray crystallographic study of several hemoglobins (*30*) that follows the sequence of ligand-binding-induced changes occurring within the T state upon ligation revealed direct

---

[†] This work was supported by National Institutes of Health grants PO1 GM-58890 and R01 EB-00296 and the W. M. Keck Foundation.

* To whom correspondence should be addressed. Tel: 718-430-3591. Fax: 718-430-8819. E-mail: jfriedma@aecom.yu.edu.

[1] Abbreviations: HbA, adult human hemoglobin; CO, carbon monoxide; deoxy, deoxygenated or ligand-free; LT, low-affinity T.; HT, high-affinity T.; VRR, visible resonance Raman; UVRR, UV enhanced resonance Raman; MEM, maximum entropy method; GR, geminate recombination, GR.; XL, cross-linked; IHP, inositol hexaphosphate.

10.1021/bi050010i CCC: $33.50

evidence for a range of accessible conformations associated with the ligated T-state species. On the basis of crystallographic parameters, populations were also divided into low-affinity T (LT) and high-affinity T (HT) populations. The present study directly complements the crystallographic study by probing both functional and conformational properties of LT and HT species in both solution and sol−gel.

The current study extends two earlier works: one that used solution-phase and sol−gel-encapsulated Fe−Zn hybrids of HbA to probe T-state conformational plasticity (*31*) and the other that probed the conformational and kinetic properties of the low- and high-affinity T state forms of encapsulated HbA (*32*). In the present study, the scope of the T-state landscape is more broadly explored. Two mutants of HbA are used to access, both in solution and in sol−gel, a range of stable functional forms of the T state even when fully ligated. The Hb(Nβ102A) mutant is used to access the lower-affinity range of the T-state conformational distribution, whereas αXLHb(Wβ37E), the Lys α99 diaspirin cross-linked form of the Hb(Wβ37E) mutant, provides access to the high-affinity T state conformations. The conformational and functional properties of these mutant forms are compared with the range of T-state properties observed for fully ligated encapsulated HbA and partially ligated Fe−Zn hybrid forms of HbA both in solution and in sol−gel. The maximum entropy method (MEM) is used to group and compare kinetically distinct populations, thus allowing for a direct comparison of accessible T states among the species derived from the above hemoglobins.

The Hb(Nβ102A) mutant had been shown to bind oxygen with reduced cooperativity and very low oxygen affinity (*26*, *33*). Replacement of the β102 asparagine with alanine eliminates the Asp $\alpha_1$94−Asn $\beta_2$102 hydrogen bond, a crucial interaction contributing to the stability of the R quaternary state, without perturbing the key interactions associated with T-state stability. It has been demonstrated that the crystal structure of the deoxy derivative of this mutant is identical to that of the deoxy HbA and that the oxygen titration for this crystal reveals an extremely low P50 ($>$100 mm) comparable to that associated with the binding of oxygen to the T-state crystals of deoxyHbA (*26*). Most significant is the absence of significant functional heterogeneity between α and β chains within the Hb(Nβ102A) tetramer (*34*). Furthermore, in more recent findings (Kwiatkowski, Karasik, and Noble, private communication), Hb(Nβ102A), either in the presence of IHP or with a cross-linking ($\alpha\alpha$- diaspirin) modification, binds oxygen noncooperatively ($n = 1$) with an extreme low affinity (P50 > 100) that is comparable to what is observed in oxygenation studies on crystals of the deoxy T-state form of both this mutant and HbA (*26*). The results indicate that (i) the mutant adopts the same deoxy T state as HbA, both with respect to structure and functional properties and (ii) under solution conditions, the mutant exhibits functional properties indicating that it remains in the T state after ligand binding. All indications are that this mutant is an excellent model for accessing ligand-binding-induced low-affinity T-state conformations under conditions where contributions from the R state are minimal.

Mutations at the β37 position have been shown to have a profound effect on the ligand-binding properties of the T-state tetramer that can be directly linked to a disruption of elements of the T-state tertiary structure that are associated with quaternary constraint (*24*, *25*, *35*, *36*). Quaternary constraint refers to the T-state-derived decrease in heme reactivity toward ligand binding relative to the reactivity of the isolated $\alpha\beta$ dimers. Hb(Wβ37E) shows the largest of such effects among those mutants that have been systematically examined. As with the other members of this series, the X-ray crystallographic results show that the deoxy derivative adopts the standard deoxy T quaternary structure close to that observed for HbA but that upon ligand binding accesses what has been termed a high-affinity T-state (HT) conformation (*30*). The results to date indicate that this mutant (i) upon ligand binding readily accesses the HT state and (ii) binds oxygen with little or no cooperativity. This mutation also has the added effect of destabilizing the tetramer. In the present study, the diaspirin Lysα99 cross-linked form of this mutant is used to eliminate contributions to the measurements from dimers (*26*, *34*). Aside from eliminating the potential complication of dimers, the cross linking has been shown both in this and earlier studies to have minimal impact on the unusual T-state ligand-binding properties of the mutant (*26*).

The utilization of these two mutants to explore features of the tertiary and/or quaternary structure landscape within the confines of the T state is further augmented by using sol−gel encapsulation protocols (*37*−*40*). Encapsulation allows for the generation of ligated derivatives of proteins that retain the conformational memory of the initially encapsulated deoxy derivative and only slowly evolve toward the more stable conformational distribution associated with the solution-phase ligated derivatives (*41*). The presently employed encapsulation protocol (*31*, *38*, *39*, *42*) either minimizes or, more typically, eliminates the contribution of the R state when CO is added to the initially encapsulated T-state deoxy derivative.

Resonance Raman spectroscopy is used to probe key conformational elements for the solution phase and sol−gel-encapsulated mutant hemoglobins. Visible excitation (435.8 nm) by an 8 ns pulse is used to generate the Soret-enhanced Raman spectra of both stable deoxy derivatives and the 8 ns deoxy-like photoproduct of CO-saturated derivatives (*43*−*45*). These photoproduct spectra reflect the impact of the initial prephotodissociation conformation of the CO derivative on the resulting five-coordinate high-spin ferrous heme. The frequency of the iron−proximal histidine stretching mode (referred to as ν(Fe−His**)** in the subsequent text) is a direct probe of quaternary constraint within the T state (*43*−*50*). This frequency correlates directly with CO rebinding kinetics (*31*, *32*, *43*−*45*, *51*, *52*). UV excitation at 229 nm is used to generate Raman spectra resonantly enhanced by the absorption of aromatic amino acid chromophores, especially tryptophan and tyrosine (*53*−*56*). The well-characterized 229 nm UV resonance Raman spectrum from HbA contains tyrosine and tryptophan bands that are highly sensitive to functionally and conformationally important domains within the $\alpha_1\beta_2$ interface (*57*−*67*).

The functional properties of hemoglobins are probed through the geminate (*68*−*71*) and bimolecular CO rebinding kinetics that occur after the photodissociation of the CO derivative using an 8 ns excitation. The resulting kinetics are analyzed through the maximum entropy method to help identify distinct kinetic populations based on distinct distributions of bimolecular rebinding rates in the pseudo-first-order limit. The results clearly reveal multiple discrete T-state populations that are functionally and conformationally distinct. These different T-state populations are apparent, albeit with varying amplitudes, in both HbA (including the Fe−Zn hybrids) and the two mutants. The spectra and kinetics provide clear insight into the origin of the range of reactivity associated with T-state hemoglobins and provide distinct markers for LT and HT populations. Most significantly, the results show that all of the above Hb's can access the same kinetically distinct high- and low-affinity ligated T-state populations, which also validate the use of the above two mutants as model systems suitable for probing the T-state conformational landscape.

MATERIALS AND METHODS

Materials. All materials, including inositol hexaphosphate (IHP) and tetramethyl orthosilicate (TMOS), were commercially obtained at the highest purity available. The potent allosteric effector 2,[4-([(3,5-dichlorophenyl)amino]carbonyl amino)phenoxy]-2-methylpropanoic acid (L35) (*72*) was obtained as a gift from Dr. I. Lalezari. Human hemoglobin was purified as described previously (*73*). The cross linked derivative of the Hb(β102A) mutant was prepared from α dimers cross-linked between the α99 lysine residues using the methods of Chatterjee et al. (*74*) and Snyder et al. (*75*, *76*) and of the mutant Hb(βW37E) as described by Kwiatkowski et al. (*25*).

Sol−Gel Encapsulation. We employed a sol−gel encapsulation protocol that has been shown in previous studies to exhibit a high degree of locking in of the conformational structure (*31*, *38*, *39*). When referring to the samples, we use a notation that indicates the history of the samples as shown in the scheme below. Square brackets are used to indicate the species and conditions present during the sol−gel encapsulation and aging. Any changes to the samples after gelation and aging (e.g., the addition of a ligand or a change in bathing buffer) appear on the outside and to the right of the square brackets with subsequent additions added on to the right. All of the buffers and solutions were deoxygenated prior to gelation. The deoxy HbA stock was generated by nitrogen purging and reduction with dithionite. Anaerobic conditions were maintained at all steps prior to CO addition. UV−vis measurements were taken before and after gelation to verify the ligation and oxidation state of the samples. The bathing buffer was 50 mM BisTris acetate and 25% glycerol in volume at pH 6.5. The final protein concentration in the sol−gel samples was ~0.5 mM in heme.

Protocol 1, Trapping the COHb equilibrium population

$$\text{COHb}\pm\text{effectors} \xrightarrow{\textit{gelation \& aging}} [\text{COHb}\pm\text{effectors}]$$

Protocol 2, Trapping the deoxyHb equilibrium population

$$\text{deoxyHb}\pm\text{effectors} \xrightarrow{\textit{gelation \& aging}} [\text{deoxyHb}\pm\text{effectors}] \xrightarrow{\text{CO exposure}} [\text{deoxyHb}\pm\text{effectors}]\text{+CO}$$

Experimental Procedures. To improve locking in, that is, the minimizing of the relaxation of nonequilibrium populations trapped within the sol−gel, the samples were kept at ~4 °C. The clock is started by a rapid addition of CO to the sol−gel-encapsulated samples. CO binding to heme is monitored using UV−vis spectra. Typically the Hb sample converts to the fully carbonmonoxy derivative within 5 min of addition of the CO-saturated buffer. Then the samples are subjected to a battery of spectroscopic and kinetic measurements.

Visible Resonance Raman Spectroscopy. Visible resonance Raman (VRR) spectra were generated using an 8 ns pulsed laser at 435.8 nm (obtained using a hydrogen-filled Raman cell to Raman shift 532 nm pulses of an Nd:YAG laser (Continuum, Santa Clara, CA). A detailed description is available elsewhere (*31*, *38*, *39*, 77).

UV Resonance Raman Spectroscopy. UV-enhanced resonance Raman spectra (UVRR) were generated using a continuous wave (CW) laser at 229 nm as described previously (*31*, *59*, *60*, *78*).

CO Rebinding Kinetics. CO recombination measurements were carried out by following the transient absorption of the sample at 442 nm. Excitation with 8 ns pulses at 532 nm at 1 Hz from an Nd:YAG laser (Minilite, Continuum, Santa Clara, CA) was used for the CO photodissociation. A greatly attenuated CW laser at 442 nm was used as the probe. A detailed description of the apparatus is available elsewhere (*31*, *59*, *60*, *78*−*80*).

Maximum Entropy Method (MEM). Kinetic traces were deconvoluted using maximum entropy analysis as a means of identifying and grouping kinetic populations as a function of solution conditions, protein modification, time, and degree of ligation. This treatment calculates lifetime distributions without any a priori assumptions about the shape of the distribution and is therefore model independent. MEM is especially well suited for an analysis of the complex multidecade traces generated in the present study. The use of MEM to extract kinetic constants associated with ligand rebinding in a range of hemeproteins is well established (*81*−*86*). The MEM analysis was performed using a previously described algorithm (*87*, *88*) that is now part of a commercially available package contained within the analysis module in Felix 3.2 software (Photon Technology International, Lawrenceville, NJ). Our results are consistent with the data obtained in earlier applications. Kinetic data generated by photolysis were analyzed by setting a maximum number of anticipated lifetimes and expected lifetime limits and by limiting the χ^2 value to 1. Distribution moments and related parameters were evaluated to determine the shape of the resulting distributions. Fits to the data were performed several times using different lifetime limits. In each case, the autocorrelation was centered at zero (±0.1), which is considered an acceptable fit. In addition, the residuals were unstructured and randomly distributed about zero. From these statistical parameters, changes in the distribution were estimated to be within 5−15%. The robustness of the analysis was further tested by increasing χ^2 to >1 and monitoring the extent to which the number of peaks and peak positions varied. All of the peaks discussed in the present treatment showed minimal variation with respect to center position and relative amplitude. The reported peaks represent Gaussian distributions of lifetimes. The center points are the mean values of the Gaussian distributions. The half width of the peaks represent ±1 standard deviation, which is similar to

Table 1: Visible Resonance Raman Data[a]

		deoxy			CO		
protein		+ IHP	+ IHP + L35		+ IHP	+ IHP + L35	
HbA	214			230	228	224	
αZn/βFe	220	220	220.5			222.5	
βZn/αFe	205					221	
XLβ37E	217.5	217.5		224.5	224	224	
XLαZn βW37E	222.5			224.5	224.5		
XLβZn βW37E	216.6			225	224.5		
βN102A		214		226.5	223	221.5	
[dxXLβW37E]		218.5					
[COXLβW37E]				224.5	224.5		
[dxXLβW37E]+CO				224.5	224.5		
[COβN102A]					223		
CO addition timeline	no CO	1 hour	2 days	9 days	14 days	36 days	5 months
[dxβN102A+IHP]	214	217	217.5	218	219	219.5	223.5

[a] Fe−His Band Peak Position (cm^{-1})

Table 2: MEM-Generated Bimolecular CO Recombination Lifetimes for Hemoglobins in Solution and Sol−Gel under Pseudo-First Order Conditions

sample[a]	R (μs)	HT (μs)	LT3 (ms)	LT2 (ms)	LT3 (ms)
COHb	140 (1.0)				
[COHb]	280 (1.0)				
[COHb + IHP]	235 (0.71)	630 (0.29)			
COHb(Nβ102A)		356 (1.00)			
COHb(Nβ102A) + L35		414 (0.53)	7 (0.11)	37 (0.35)	
COHb (Nβ102A) + IHP		825 (0.49)	13 (0.18)	43 (0.33)	
COHb (Nβ102A) + IHP + L35		708 (0.29)	∼2(sh)	27 (0.33)	89 (0.38)
[COHb(Nβ102A) + IHP]		420 (0.28)	2.5 (0.38)	33 (0.33)	
[dxHb (Nβ102A) + IHP]			2.0 (0.39)	14 (0.32)	55 (0.28)
COXLHb(Wβ37E)			1.0 (1.0)		
COXLHb(Wβ37E) + IHP			2.5 (1.0)		
[COXLHb(Wβ37E) + IHP]		455 (1.0)			
[dxXLHb(Wβ37E) + IHP]		695 (0.64)	1.3 (0.35)		
[COHb(Wβ37E:αZn/βFe) + IHP]		750 (0.52)		17 (0.48)	
[dxHb(Wβ37E:αZn/βFe) + IHP]		675 (0.12)	2.4 (0.17)	17 (0.71)	
[COHb (Wβ37E:αFe/βZn) + IHP]		630 (0.29)		16 (0.71)	
[dxHb(Wβ37E:αFe/βZn) + IHP]			2.5 (0.34)	25 (0.66)	
[dxHb, aged] + CO			1.2 (0.25)	11 (0.43)	56 (0.31)
[dxHb, LT] + CO		564 (0.39)		22 (0.17)	
[dxHb, HT] + CO	202 (1.0)				
[dxHb + IHP + L35] + CO					
day 1[b]		768 (0.12)		11 (0.20)	44 (0.65)
day 11[b]		400 (0.55)		11 (0.24)	25 (0.22)
COHb(αZn/βFe)			1.4 (0.20)	17 (0.42)	139 (0.52)
CO Hb (αZn/βFe) + IHP				24 (0.28)	71 (0.59)
[COHb(αZn/βFe) + IHP]			1.0 (0.29)	10 (0.19)	33 (0.32)
COHb (αFe/βZn)				18 (1.00)	
CO Hb (αFe/βZn) + IHP				24 (1.00)	
[COHb (αFe/βZn)]				11 (0.90)	

[a] Square brackets indicate that the protein is encapsulated in a sol−gel. The absence of brackets indicates a solution-phase sample. (See text for detailed nomenclature; dx is used to denote deoxy.) [b] Day(s) post CO addition. Data in the table are the centerpoints of the MEM distributions; the values in parentheses represent the fraction of the normalized population for the kinetic bimolecular phase. Normalization was done for each sample on the basis of the relative amplitude of kinetic populations with bimolecular CO lifetimes greater than 100 μs.

those obtained in previous studies. Data sets were tested further by fitting the original kinetic data with a set of exponential functions using these center points as the rates and the half widths as the preexponentials. The decay curves were successfully reproduced with this treatment. The MEM program was also tested using computer-generated decay curves that were successfully fit and reproduced by the program. The results of the MEM analysis are presented as the reciprocal of the rates to have the distribution displayed on the same axis as the kinetic traces. For the MEM populations associated with the bimolecular recombination, the amplitudes were normalized to unity, and the fractional contribution of each of the populations was calculated. The fractional distributions for the bimolecular phases are included in Table 2.

RESULTS

HbNβ102A: Visible Resonance Raman Spectra Solution-Phase Results. Figure 1 shows the low-frequency region of the Soret-enhanced resonance Raman spectra of both stable and transient ferrous five-coordinate Hb's. The lowest-frequency peak shown (between 214 and 230 cm^{-1}) corresponds to the conformation sensitive iron−proximal histidine stretching mode, ν(Fe−His). The frequency of this mode is a direct reflection of proximal strain. The proximal strain is a contribution to the quaternary constraint that causes reduced

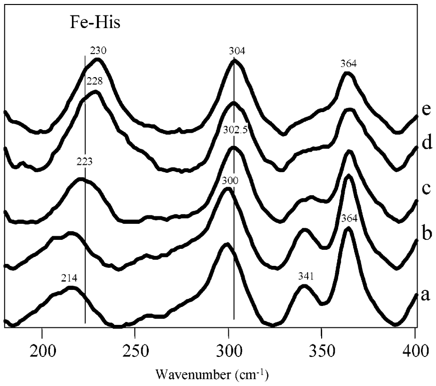

FIGURE 1: Low-frequency portion of the Soret-enhanced resonance Raman spectrum derived from (a) deoxy HbA, (b) deoxy Hb(Nβ102A) + IHP, (c) the 8 ns photoproduct of COHb(Nβ102A) + IHP, (d) the 8 ns photoproduct of COHbA + IHP, and (e) the 8 ns photoproduct of COHbA. All of the samples are in the solution phase at pH 6.5 maintained at ~4 °C.

ligand affinity in the T state. The proximal strain originates from the added T-state energy penalty associated with moving the iron into the plane of the heme macrocycle upon ligand binding (*48*).

For vertebrate hemoglobins, low frequencies for ν(Fe−His) are indicative of proximal strain, whereas high frequencies near or at 230 cm^{-1} are reflective of proximal enhancement. Proximal enhancement that is typically associated with the photoproduct of ligated hemoglobins arises from a compression of the iron−histidine bond due to the histidine being constrained by the protein to be close to the heme (*47*, *58*). As a result, there is a reduction in the energy cost associated with moving the iron in plane upon ligand binding.

The heme-γ_7-mode band at approximately 300 cm^{-1} has also been shown to be sensitive to proximal strain with lower frequencies, which is indicative of increased proximal strain (*89*). The propionate-sensitive band at 340 cm^{-1} is prominent and distinct for stable ferrous-five-coordinate hemoglobins, whereas for the early time photoproduct it is reduced in intensity and poorly defined as a discrete band, especially for the R-state photoproduct (*45*).

Spectra a and b are a comparison between the deoxy derivatives of HbA and Hb(Nβ102A)+IHP, respectively. It can be seen that the two spectra are essentially identical, resembling previously described spectra from deoxy HbA. This result is consistent with the deoxy derivative of the mutant adopting a tertiary/quaternary conformation distribution that is very similar to that of deoxy HbA.

Spectra c through e are derived from the ferrous-five-coordinate heme, generated within 8 ns of photodissociating the parent COHb. As such, the species yielding the spectra are typically transient ferrous-five-coordinate heme species that still retain the influence of the unrelaxed (or nearly unrelaxed) ligated protein conformation (*44*, *45*). It can be seen that the frequency of ν(Fe−His) increases in going from the stable deoxy forms to the photoproducts. The frequency of ν(Fe−His) for the photoproduct of COHb(Nβ102A) is lowest at 221.5 cm^{-1} in the presence of both IHP and L35 (not shown; see Table 1) and increases to 222. 5 cm^{-1} with the removal of any one of the two effectors (only the +IHP is shown in Figure 1, spectrum c). In the absence of effectors, the HbNβ102A photoproduct yields an even higher frequency at 226.3 cm^{-1} (Table 1). In contrast, the photoproduct frequencies from COHbA under similar conditions with or without IHP are 228 and 230 cm^{-1}, respectively (spectra d and e). It can be seen that the heme-γ_7-mode band follows a similar progression, although over a much narrower frequency range (300−304 cm^{-1}).

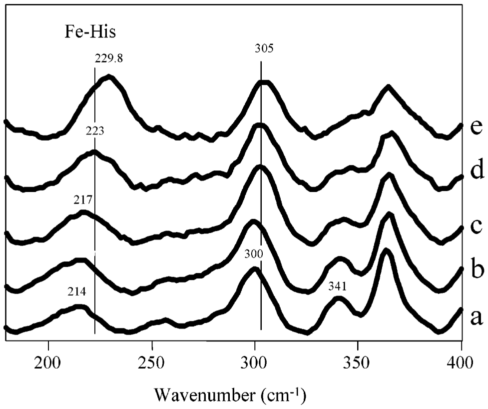

FIGURE 2: Low-frequency portion of the Soret-enhanced resonance Raman spectrum of sol−gel-encapsulated hemoglobins as a function of ligation for the Hb(Nβ102A) mutant with spectra from encapsulated HbA presented for comparison. (a) [deoxy HbA], (b) [deoxy Hb(Nβ102A + IHP], (c) [deoxy Hb(Nβ102A) + IHP] + CO after 1 h, (d) [COHb(Nβ102A) + IHP], and (e) [CO HbA].

HbNβ102A: Visible Resonance Raman Spectra from Sol−Gel-Encapsulated Samples. Figure 2 shows the same low-frequency region of the Raman spectrum as in Figure 1, but in this case, the samples are encapsulated in a porous sol−gel matrix bathed in buffer. Spectrum a, derived from sol−gel encapsulated deoxy HbA, is virtually identical to the solution-phase spectrum shown in Figure 1a. The spectrum of encapsulated deoxyHb(Nβ102A) + IHP (spectrum b), designated as [deoxyHb(Nβ102A) + IHP], is seen to be nearly identical to that of the corresponding deoxy HbA sample (spectrum a). These results indicate that at least with respect to the quaternary/tertiary structure-sensitive proximal heme pocket environment of the deoxy derivatives of both HbA and Hb(Nβ102A), the sol−gel-encapsulation protocol does not noticeably perturb the solution-phase conformations.

Spectrum c is from the 8 ns photoproduct of the sol−gel-encapsulated sample, generated within an hour of the addition of a large excess of CO-saturated, IHP-containing buffer to [deoxy(HbNβ102A)+IHP]. The visible absorption spectrum of the sample indicated that the sample converted to the CO derivative within several minutes of adding the CO-saturated buffer. Spectrum c illustrates that there is a small but relatively rapid change in conformation upon the addition of CO that results in a slight decrease in proximal strain as reflected in the small frequency increase in ν(Fe−His) and γ_7. Spectra d and e are associated with samples in which the CO derivatives, that is, [COHb(Nβ102A)+IHP] and [COHbA], respectively, were directly encapsulated. A comparison among spectra b, c, and d shows that encapsulation greatly slows the CO-binding-induced transition from the equilibrium deoxy derivative of the mutant to the ligated derivative. It takes in excess of a month for the encapsulated deoxy plus CO sample to achieve the end-point spectrum, as can be seen in the bottom of Table 1. In contrast, the corresponding deoxy turned CO-encapsulated HbA sample achieves the 222−223 cm^{-1} value within hours of the

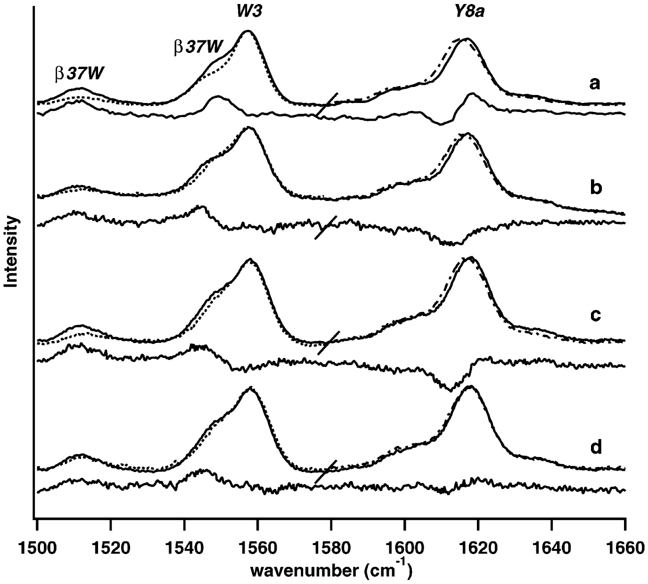

FIGURE 3: Comparison of the high-frequency portion of the 229 nm excited UV resonance Raman spectrum of deoxy (solid line) and CO (dashed line) derivatives of the following samples: (a) HbA in solution, (b) Hb(Nβ102A) + IHP in solution, (c) encapsulated deoxy and CO derivatives of Hb(Nβ102A) + IHP, and (d) encapsulated deoxy Hb(Nβ102A) + IHP before and after the addition of CO. In each instance, the deoxy CO-difference spectrum (solid − dashed lines) is shown below the two individual spectra. Both the W3 and Y8a bands have been independently normalized (hence, the back slash dividing the spectra at approximately 1580 cm^{-1}) to better demonstrate the frequency differences for each band.

addition of CO. Table 1 contains the frequencies of ν(Fe−His) for these samples as well as for related samples including Hb(Wβ37E), whose spectra are not shown.

UVRR Spectra: Overview. Whereas the visible resonance Raman results address conformational issues associated with the heme and the heme environment, the UV resonance Raman results provide details associated with the T-state constraints within the $\alpha_1\beta_2$ interface. Figure 3 shows only the high-frequency region (1500−1660 cm^{-1}) of the 229 nm excited UV resonance Raman (UVRR) spectrum (800−1680 cm^{-1}). This high-frequency region contains bands that have been well characterized with respect to specific conformational degrees of freedom associated with the hinge and switch regions of the $\alpha_1\beta_2$ interface (*57*, *61*, *67*, *90*−*93*).

Figure 3 shows the 229 nm excited resonance Raman spectra of deoxy (solid line) and CO (dashed line) derivatives and their difference spectrum (deoxy−CO) for solution-phase HbA (series a); solution-phase HbNβ102A + IHP (series b); [deoxyHbN(β102A) + IHP] and [COHb(Nβ102A) + IHP] (series c); and [deoxyHb(Nβ102A) + IHP] and [deoxyHb(Nβ102A) + IHP] + CO (series d). Note that the W3 band and the Y8a band are independently normalized with respect to their peak intensities to better expose the shift in Y8a and the intensity change in the Trp β37-associated shoulder of the W3 band. It can be seen that the deoxy T versus ligated R differences seen for HbA in series a are also in evidence for Hb(Nβ102A) but with smaller amplitudes for the latter. For both solution and sol−gel samples, the spectra of deoxy versus CO derivative of the mutant (series b and c) show a reduced shift in Y8a and reduced intensity changes both in the β37 shoulder of W3 and in the β37 sensitive 1511 cm^{-1} band. The deoxy versus ligated differences are nearly but not completely eliminated for the mutant in series d, where the encapsulated deoxy form is compared to the CO derivative generated from an initially encapsulated deoxy sample.

For series a, the difference spectrum reflects the difference between the deoxy T state and the fully ligated R state of HbA. In contrast, all of the subsequent Hb(Nβ102A) difference spectra represent comparisons between the deoxy T state and either the equilibrium population of the ligated T state (series b and c) or the T-state populations with tertiary conformations that are intermediate between the stable forms of deoxy T and ligated T (series d). It is clear from these series of difference spectra that the $\alpha_1\beta_2$ interface does not function as a simple two state switch. On the basis of the established assignments for the features in the difference spectra, the UVRR data show that upon ligand binding within the T quaternary state there is a progressive loosening of the T-state constraints within the $\alpha_1\beta_2$ interface. Similar ligand binding-induced loosening of the T-state constraints was previously noted for Fe−Zn hybrids of HbA (*31*) and [deoxyHbA] + CO (*32*).

Geminate and Bimolecular Recombination. The functional properties of the different T-state populations that were identified using Raman spectroscopy are now examined through CO-recombination kinetics after photodissociation. Whereas the combination rate measurements using mixing technology primarily probe the initial deoxy Hb population, the recombination following rapid photodissociation probes the initial population of the ligated derivative as well as populations that have undergone relaxation during the time course of the measurement. The initial geminate-recombination phase most directly correlates with the population retaining the conformational distribution of the initial ligated or photoproduct species. The slower bimolecular- or solvent-phase recombination can reflect populations that have undergone relaxation after the initial photodissociation. The use of sol−gel encapsulation minimizes the relaxation effects due to the damping of both tertiary and quaternary state relaxation on the time scale of kinetic measurements.

Figure 4 shows the range of kinetics observed for the rebinding of CO after photodissociation by an 8 ns pulse for solution-phase samples at pH 6.5. Traces a and b from COHb(αZn/βFe) + IHP and COHb(Nβ102A) + IHP + L35, respectively, show variation in the kinetic pattern for the T-state species. The initial rebinding occurring throughout the nanosecond to early microsecond time regime has been identified as geminate recombination (*68*, *69*, *71*). The two recombination phases observed for COHbA and shown in trace c, occurring between 100 μs and 1 s, correspond to the bimolecular rebinding of CO molecules from the solvent (*94*). The fast and slow bimolecular phases correspond to R- and T-state combination rates, respectively. Trace d is also derived from COHbA but under conditions of low photolysis that greatly reduce the conversion of the photoproduct to the T-state population. As a consequence, there is no T-state bimolecular rebinding phase in the kinetic trace, and only the R-state bimolecular phase is seen. All subsequent traces were obtained under essentially the same, low photolysis excitation limit. The rebinding kinetics from COHb(Nβ102A) + IHP + L35 shown in trace b reveal a marked decrease in the geminate yield, an absence of the R-state bimolecular phase, a sizable population displaying

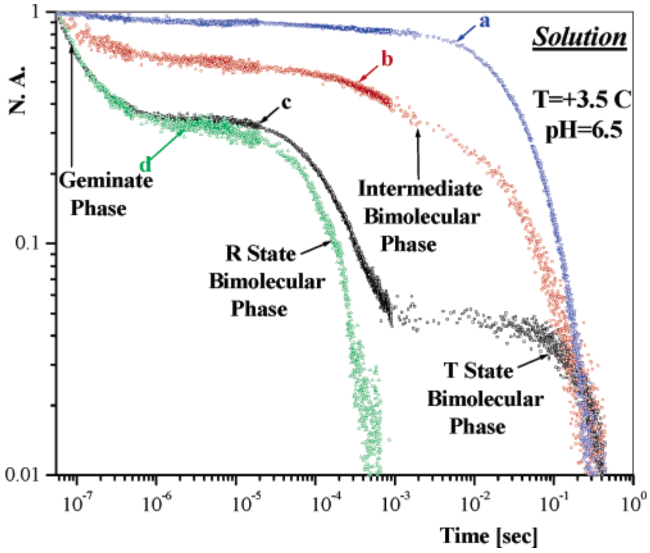

FIGURE 4: Traces depicting CO rebinding to photodissociated CO-saturated hemoglobin derivatives at pH 6.5 at 3.5 C in solution displayed on a log−log plot of normalized absorbance vs time for the following samples: (a) COHbA(αZn/βFe) + IHP, (b) COHb-(Nβ102A) + IHP and L35, (c) COHbA under a high photodissociation limit, and (d) COHbA in the low photodissociation limit. Except for trace c, all traces were generated under low photodissociation conditions (no difference between the high and low limits for traces a and b).

the T-state bimolecular phase, and what appears to be an intermediate phase occurring between the T-state and R-state bimolecular phases shown in trace c. Trace a, which was previously discussed in an earlier work (*31*), is derived from a species that has been designated as an extreme T state. It shows a geminate yield of near zero and no indication of an intermediate T state kinetic phase. The reduced geminate yields and T-state bimolecular phases shown in traces a and b are consistent with previously reported patterns derived from T-state CO derivatives of iron−metal hybrids of HbA (*31*, *95*).

The next several figures depict recombination traces and the corresponding MEM-derived kinetic populations associated with the bimolecular recombination under pseudo-first-order conditions (high CO-to-heme ratio).

Figure 5 shows the rebinding kinetics (a) and the corresponding MEM analysis (b) for solution-phase COHb-(Nβ102A) as a function of added effectors. The MEM populations, displayed as the reciprocal of the rebinding rate, are divided into two major groupings. The faster groups that appear between 10^{-9} and 10^{-5} s contain the kinetic phases associated with geminate recombination. The slower grouping that appears between 10^{-4} and 10^{0} s contains those kinetic phases/populations associated with the so-called solvent or bimolecular recombination phases. The distinct peaks shown in the MEM-derived traces are referred to as kinetic populations to aid in distinguishing and classifying distinct groupings of kinetic constants. Several of the traces yield MEM-derived populations that are between the geminate and bimolecular populations. These intermediate peaks are not as yet assigned but, on the basis of similar studies on myoglobin mutants (*86*, *96*), appear to be associated with rebinding from remote sites in the protein under conditions where the side chains of the distal hemepocket have not fully relaxed and water has not reoccupied the vacated distal hemepocket. These peaks and their assignment have no bearing on the assessment of T-state populations, which is based on the distribution of pseudo-first-order rate constants

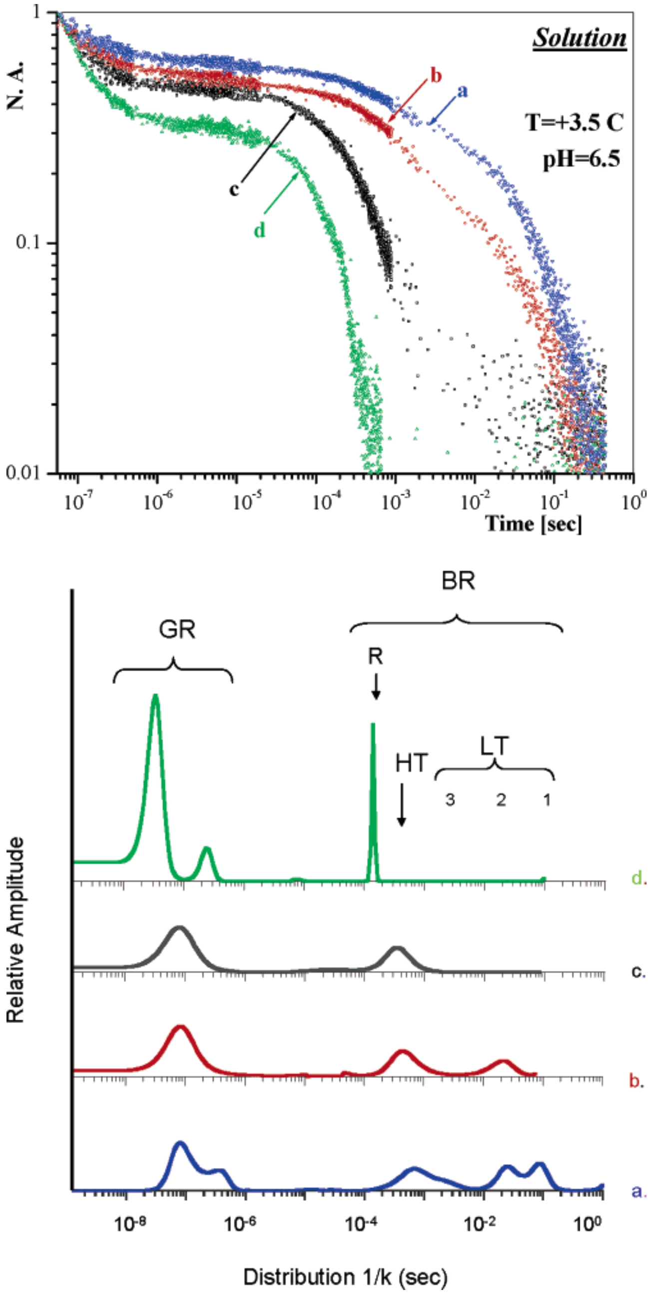

FIGURE 5: (a) CO recombination on a log−log plot for solution-phase samples in the low photodissociation limit. Trace a: COHb-(Nβ102A) + IHP + L35, trace b: COHb(Nβ102A) + L35, trace c: COHb(Nβ102A), and trace d: COHbA. See text for experimental details. (b) MEM (maximum entropy method) kinetic populations displayed as $^{1}/_{k}$ on a log−time scale derived from CO rebinding traces from the following solution phase samples. Series a: COHb-(Nβ102A) + IHP + L35, series b: COHb(Nβ102A) + L35, series c: COHb(Nβ102A), and series d: COHbA. The kinetic populations are grouped into two categories: geminate recombination (GR) and bimolecular recombination (BR). The focus of the present study is primarily on the BR (bimolecular recombination) populations that have been subdivided into an R state (R), three LT (low-affinity T state), and one HT (high-affinity T state) population. As can be seen in Table 2, each of the LT and HT categories covers a range of values. The labels provide a rough indication of where each of these variable populations appears. The origin and nature of the multiple geminate and intermediate phases (between 10 and 100 μs) shown are the focus of a future paper.

derived from the solvent-phase bimolecular recombination processes. The multiple geminate phases as well as the intermediate phases are the focus of a future manuscript. T-state bimolecular populations are further subdivided into high-affinity T (HT) and three low-affinity T (LT) populations. These groupings arise in part from the clustering of kinetic values obtained from the MEM analysis, which are provided in Table 2.

A clear pattern with respect to the added effectors to the Nβ102A mutant is shown in Figure 5a and b. With the addition of effectors, the geminate yield decreases and the bimolecular recombination gets slower. In each instance, the kinetic trace is clearly not made up of a simple sum of T and R as seen for HbA in trace c of Figure 4. The MEM-derived kinetic populations that correspond to each trace in Figure 5a are shown in Figure 5b. In Figure 5b, trace a shows that in the presence of both IHP and L35 the bimolecular rebinding contains contributions from all four T-state kinetic populations (LT3 is seen as a shoulder (noted as (sh) in Table 2) on the slow side of the HT population. In the presence of only L35 (essentially the same trace with either IHP or L35), as shown in trace b, the population is now skewed further toward HT with a loss of LT1 and LT3. Trace c shows that in the absence of added effectors the bimolecular phase is dominated by HT, which can (vide infra) be consistently differentiated from the slightly faster R population observed for COHbA (trace d). The Figure also shows that in going from a to d there is a progression of increasing relative amplitudes for the geminate phase with respect to the bimolecular phases.

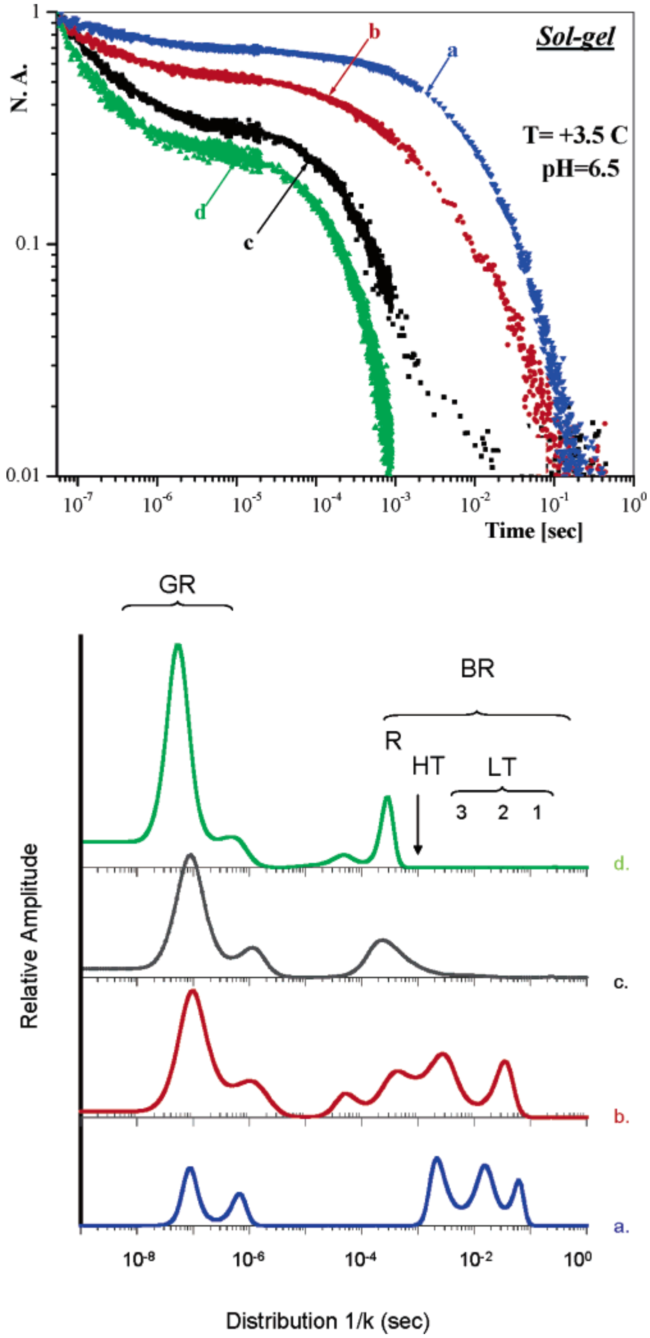

FIGURE 6: (a) CO recombination on a log−log plot for encapsulated hemoglobin samples in the low photodissociation limit. Trace a: [deoxyHb(Nβ102A) + IHP] + CO, trace b: [COHb(Nβ102A) + IHP], trace c: [COHbA + IHP], and trace d: [COHbA]. See text for nomenclature and experimental conditions. (b) MEM (maximum entropy method) kinetic analysis displayed as $^1/_k$ on a log−time scale derived from CO rebinding traces from the following samples. Series a: [deoxyHb(Nβ102A) + IHP] + CO, series b: [COHb(Nβ102A) + IHP], series c: [COHbA + IHP], and series d: [COHbA].

Figure 6 parts a and b display the kinetic traces and corresponding MEM analyses from sol−gel-encapsulated samples of Hb(Nβ102A) and HbA. Trace d, from HbA, is similar to the R-state pattern seen from the solution phase but with an enhanced geminate yield due to the sol−gel (+25% glycerol)-induced increase in local viscosity (*38*, *97*) and with a slow down in the R-state bimolecular phase. Also shown is the kinetic trace (trace c) for [COHbA + IHP] at pH 6.5. It can be seen that compared to [COHbA] there is a reduction in the geminate yield, as is also seen in solution (*52*), and a broadened R-state bimolecular rate that is now skewed toward slower rates that the MEM shows to arise from a contribution from an HT population. At the extreme other end of the progression is trace a from [deoxy(Nβ102A) + IHP] + CO, which resembles previously reported T-state traces from [deoxyHbA] + CO (*32*, *38*, *97*, *98*) and CO-saturated Fe−Zn hybrids of HbA in either solution (plus effectors) or sol−gel matrixes (*31*). The trace from the corresponding encapsulated sample derived from the encapsulation of the CO derivative, that is, [COHb(Nβ102A) + IHP] is shown as trace b. It can be seen that relative to trace a from [deoxy(Nβ102A) + IHP] + CO the geminate yield is enhanced and the bimolecular phase is faster. Traces a and b in Figure 6b show that the MEM populations display a loss of the HT peak and a clear skewing of the rates toward the LT populations for [deoxyHb(Nβ102A) + IHP] + CO vis-à-vis [COHb(Nβ102A)] + IHP. This result is consistent with encapsulation locking in the initial conformational distribution, and as a consequence, the [COHb] and [deoxyHb] + CO samples will manifest the functional and spectroscopic properties of ligand-saturated and ligand-free distributions of conformations, respectively. From Table 2, it can also be seen that when comparing the same COHb(Nβ102A) + IHP sample in solution and in sol−gel the kinetic phases for the encapsulated sample are faster, as is clearly seen for the HT population (420 vs 825 μs). These differences are explainable in terms of the sol−gel limiting the extent of tertiary relaxation after photodissociation, and as a consequence, the rebinding kinetics are reflective of the initial more reactive conformation for the CO derivative. In contrast, the solution-phase sample will undergo tertiary relaxation that will slow the relaxation process (*99*).

Kinetic traces and a corresponding MEM analysis for the CO recombination of a series of encapsulated samples of XLHb(Wβ37E) are shown in Figure 7 a and b. It can be seen that for XLHb(Wβ37E), the kinetic distribution for both encapsulated CO + IHP (trace c) and encapsulated deoxy + IHP turned CO (trace b) both manifest kinetic populations heavily skewed toward the HT regime with the latter showing evidence of a minor contribution from LT populations. It can be seen in Table 2 that the corresponding solution-phase samples for the CO derivatives with and without IHP manifest slower kinetic traces with a single, broad kinetic population in the LT3 regime. This difference between the solution and sol−gel samples is again explainable in terms of the rate of fast tertiary relaxation after photodissociation as discussed above for COHb(Nβ102A) + IHP.

In contrast to fully ligated solution-phase and encapsulated samples of XLHb(Wβ37E) whose kinetic traces primarily contain the LT3 or HT populations, respectively, the encapsulated half-ligated Fe−Zn hybrids of the derivatives of XLHb(Wβ37E) manifest kinetic traces that contain a contribution not only from HT and LT3 but also from the slower LT2. This effect is shown in representative trace a in Figure 7b and in Table 2. It can be seen in Table 2 that the distribution of kinetic populations for the deoxy turned CO derivative for each of the Fe−Zn hybrids of this mutant has a higher fraction of LT populations than that of the corresponding CO-encapsulated derivative. Thus, there is a clear progression in going from symmetrically half-ligated to fully ligated derivatives of this mutant with respect to accessing the HT population. The results also indicate that for this hemoglobin, unlike Hb(Nβ102A) and HbA (vide infra), sizable LT populations cannot be generated for encapsulated samples of fully ligated derivatives, even when starting with [deoxyXLHb(Wβ37E)]. For this mutant, sizable LT populations can only be achieved when encapsulating partially ligated derivatives. The results are consistent with the barrier for the ligand-binding-induced accessing of the HT population being much lower than that for HbA or Hb-(Nβ102A), as also implied from crystallographic studies (*30*).

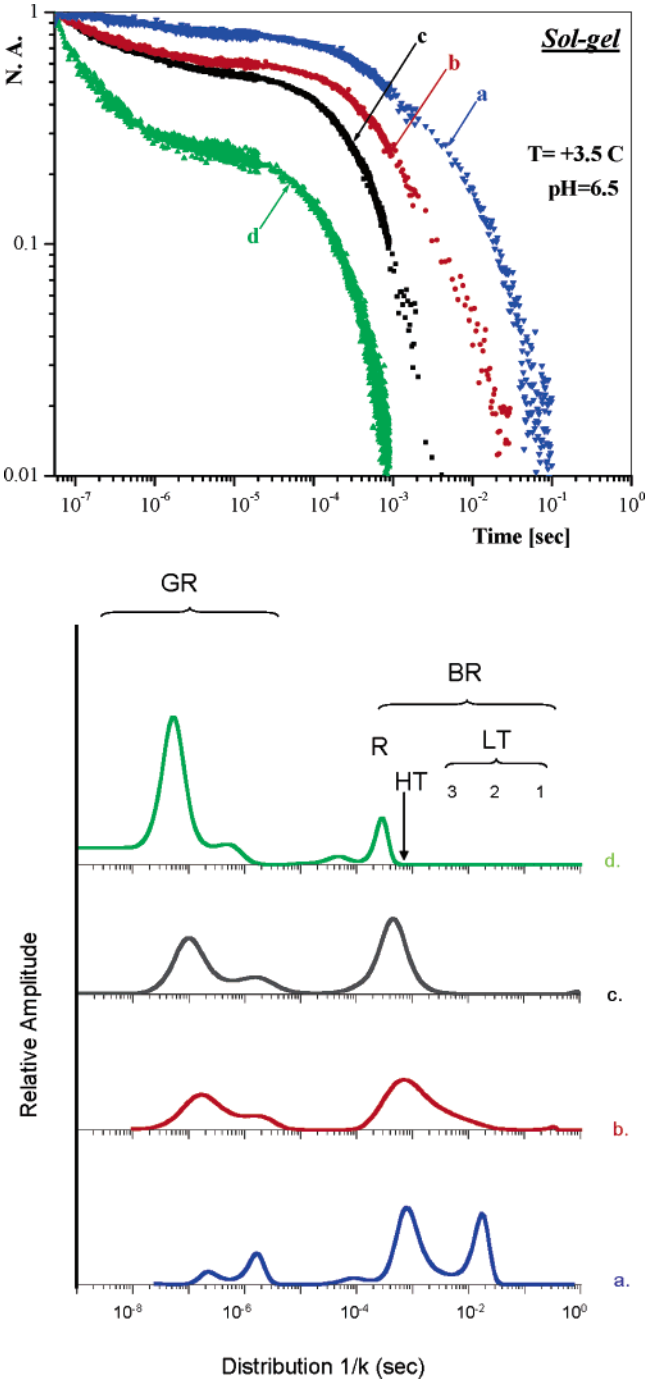

FIGURE 7: (a) CO recombination on a log−log plot for encapsulated hemoglobin samples in the low photodissociation limit. Trace a: [COHb(Wβ37E/αZn/βFe) + IHP], trace b: [deoxyXLHb(W(β37E) + IHP] + CO, trace c: [COXLHb(Wβ37E) + IHP], and trace d: [COHbA]. See text for nomenclature and experimental conditions. (b) MEM (maximum entropy method) kinetic analysis displayed as 1/*k* on a log−time scale derived from CO rebinding traces from the following sol−gel encapsulated samples. Series a: [COHb-(Wβ37E/αZn/βFe) + IHP], series b: [deoxyXLHb(W(β37E) + IHP] + CO, series c: [COXLHb(Wβ37E) + IHP], and series d: [COHbA].

The question arises as to whether HbA can access the same HT/LT kinetic populations observed for either Hb(Nβ102A) or Hb(Wβ37E). Figure 8 parts a and b display several representative traces and MEM populations derived from [deoxyHbA] + CO. Trace a is derived from a [deoxyHbA] + CO sample that was allowed to age for an extended period prior to the addition of CO (labeled [dxHb aged] + CO in Table 2). The MEM analysis clearly reveals the three LT populations that are also evident in the corresponding Hb(Nβ102A) traces. Trace b is derived from a sample prepared using a protocol (*32*) that allows for a slightly more rapid evolution of conformation upon the addition of CO (labeled [dxHb, LT] + CO in Table 2). The corresponding MEM analysis reveals a substantial HT component. Trace c is derived from a sample prepared using a protocol (*32*) that allows for a much more rapid conformational evolution. This sample was allowed to extensively evolve over time (labeled [dxHb, HT] + CO in Table 2). It is a near end-point trace, where the sample has achieved the rebinding phase associated with the R state. Table 2 contains the MEM populations from these deoxy turned-CO-encapsulated HbA samples as well as those derived from a [deoxy HbA + IHP + L35] + CO sample 1 and 11 days after the addition of CO. The pattern shows the evolution of the HT population toward faster rates and increasing amplitude at the expense of the LT populations. The range of rates for the HT population derived from

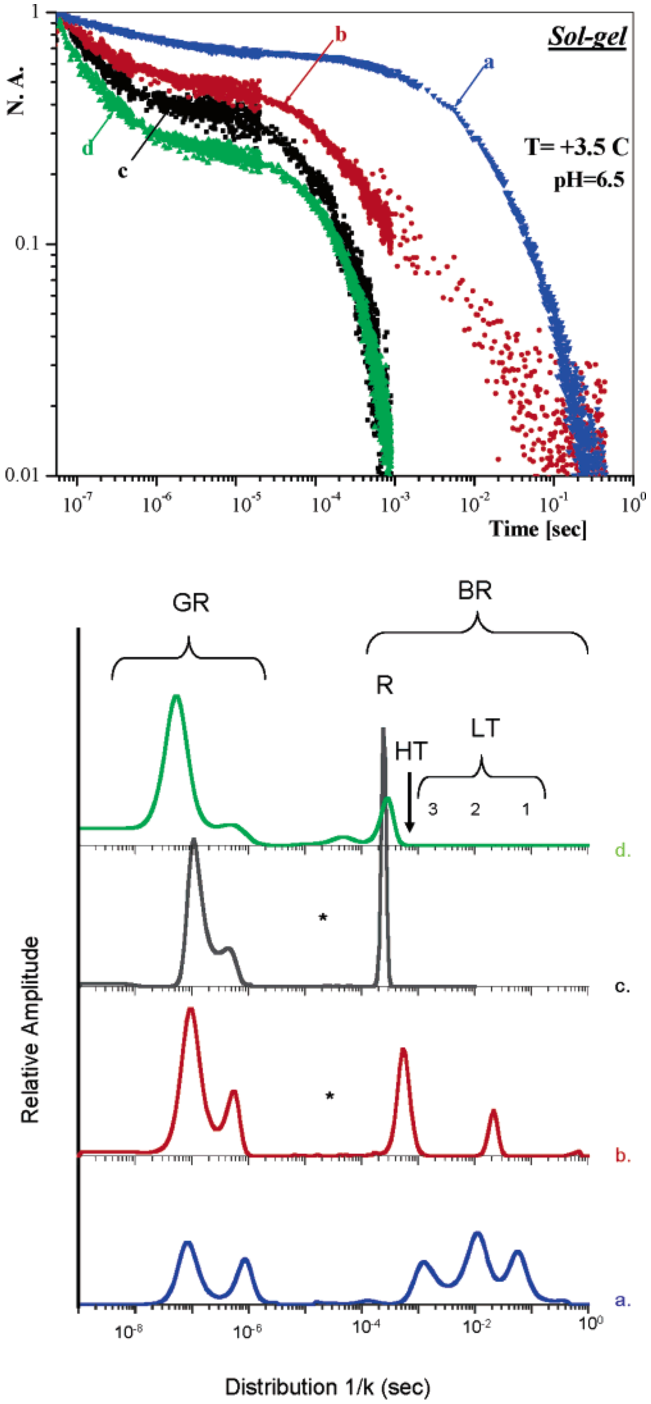

FIGURE 8: (a) CO recombination on a log−log plot for [deoxy HbA] + CO as a function of the preparative protocol. Trace a: [deoxyHbA] + CO, the sample was extensively aged prior to the addition of CO; trace b: [deoxyHbA] + CO, prepared using the LT protocol (*32*); trace c: [deoxyHbA] + CO, prepared using the HT protocol (*32*), and the trace was generated one month after the addition of CO; and trace d: [COHbA]. See text for nomenclature and experimental conditions. (b) MEM (maximum entropy method) kinetic analysis displayed as 1/*k* on a log−time scale derived from CO rebinding traces from [deoxyHbA] + CO samples as a function of time after the addition of the CO. Series a: [deoxyHbA] + CO, the sample was extensively aged prior to the addition of CO; series b: [deoxyHbA] + CO, prepared using the LT protocol (*32*); series c: [deoxyHbA] + CO, prepared using the HT protocol (*32*), and the trace was generated one month after the addition of CO; and series d: [COHbA]. See text for nomenclature and experimental conditions. The asterisks designate a region where a peak was cosmetically removed (see text).

[deoxyHbA] + CO samples covers the range seen for the various preparations of the two mutants discussed above.

Table 2 also contains the MEM analysis of previously reported (*31*) kinetic traces from half-ligated Fe−Zn hybrids in solution and in sol−gel. None of the traces manifest HT populations. For the αZn/βFe hybrids, the addition of allosteric effectors shifts the distribution toward the slower LT populations, whereas for the αFe/βZn hybrids, the addition of an effector merely slows the single LT2 population. As with the mutants, encapsulation results in distributions that are consistent with a slowing of tertiary relaxation as reflected in the presence of faster populations when compared to the corresponding solution-phase sample.

A comparison of the MEM-derived populations shown in Table 2 shows that the MEM populations observed for CO rebinding kinetics from Hb(Nβ102A) and Hb(Wβ37E) are also observed for either HbA intermediates trapped in sol−gel or partially ligated HbA derivatives. An essential difference is that the various combinations of HT and LT populations are readily stabilized for the tetra-ligated CO derivatives of the two mutants, whereas for HbA, accessing these ligated T-state populations requires either the trapping of intermediates via the sol−gel or partial ligation via the symmetric Fe−Zn hybrids.

DISCUSSION

Conformational Variability within the Deoxy T State of Hb. The present study as well as several earlier studies (*31*, *32*, *52*) shows that the frequency of the ν(Fe−His) band for deoxy HbA is stable at ∼214−215 cm^{-1}, regardless of whether effectors are present or absent. Thus, it is reasonable to assume that this frequency, also seen for the deoxy derivative of Hb(Nβ102A), is indicative of one end point for accessible T-state conformations. This stable end-point spectrum of the equilibrium population of deoxy HbA is associated with a UV resonance Raman spectrum that indicates that the T-state constraints associated with the hinge and switch regions of the $\alpha_1\beta_2$ interface are fully intact.

Deviations from this end-point deoxy T-state spectrum are not commonly seen for deoxy derivatives of most cooperative hemoglobins but are invariably seen for those deoxy T-state Hbs with chemical or mutagenic disruptions to the so-called Trp β37 cluster of residues in the hinge region of the $\alpha_1\beta_2$ interface (*26*, *35*). The hydrogen bond network that couples these residues stabilize a conformational arrangement that keeps the indole of $\beta_2$37W rigidly locked in its standard deoxy T-state position. Perturbations that loosen the packing of the β37 side chain result in an increase in the frequency of ν(Fe−His) as seen for HbMontefiore (Dα126Y) (*100*), desArg (α141)Hb (*64*, *101*), and mutants of HbA in which Tyr α140 is replaced with Phe, Ala, or Gly (*93*). This effect was most compellingly demonstrated for a series of deoxy β37-Hb mutants in which the X-ray crystallographic data showing a progressive loosening of the hinge region within the T-quaternary state correlated with the progressive increase in the frequency of ν(Fe−His) (*36*), which likely correlates with changes in the influence of Tyr α140 on the proximal heme linkage (*93*). In the present study, the deoxy derivative of XLHb(Wβ37E) falls into that category, having a frequency of ∼218 cm^{-1} for ν(Fe−His), both in solution and in sol−gel.

Conformational Properties of the Liganded T state. A ν(Fe−His) frequency of ~222 cm^{-1} is observed for the 8 ns photoproduct of COHb(Nβ102A) in the presence of effectors at low pH. A similar frequency is seen for the early time photoproduct of ligated hemoglobin derivatives that have been unambiguously assigned as T-state species. These would include NOHbA + IHP at low pH (*43*, *46*), COHb-Kansas + IHP at low pH/high concentration (*102*), and COFe−Zn hybrids of HbA in the presence of allosteric effectors at low pH (*31*). For the Hb(Nβ102A) mutant, as with the Fe−Zn hybrids and NOHbA, these conditions eliminate cooperativity and yield a very low affinity T state species. This frequency is again observed for the photoproduct of [deoxyHbA] + CO, shortly after the addition of CO (*32*, *42*) under conditions where the resulting sample has functional properties characteristic of what has been termed the low-affinity T state (*28*, *32*). In the present study, it is seen that under similar encapsulation conditions the [deoxyHb(Nβ102A)] + CO samples yield frequencies that are initially intermediate between that of the deoxy derivative (214 cm^{-1}) and end-point values that are close to those of the above-mentioned ligated T-state species. Similar intermediate values are seen (unpublished results) for [deoxyHbA] + CO under conditions where the bathing buffer for the gel is extremely viscous. Thus, for hemoglobin populations that are designated as low-affinity T state, there is a bounded range for the frequency of ν(Fe−His) that starts at 214 cm^{-1} for the deoxy derivatives and ends at ~222 cm^{-1} for the photoproduct of the ligated derivatives.

The photoproduct of ligated hemoglobins that are assigned as high-affinity T-state species exhibit a frequency for ν(Fe−His) that is higher than that seen for the low-affinity T-state species. Previously, this higher frequency was demonstrated for [deoxyHbA] + CO samples that were prepared using an encapsulation protocol that produces HT populations (*32*). In the present study, the high-affinity T-state populations derived from encapsulated Hb(Wβ37E) also yield the higher frequency at ~225 cm^{-1}.

The UV resonance Raman results obtained in the present study as well as earlier studies on Fe−Zn hybrids (*31*), encapsulated HbA (*32*), and α140Y mutants of HbA (*93*) also exhibit a progression that tracks with the decrease in proximal strain. With decreasing proximal strain (as reflected in the increasing frequency of ν(Fe−His)), the UVRR spectra show a weakening of the T-state markers associated with the $\alpha_1\beta_2$ interface with the most systematic behavior associated with the hinge region, as reflected in the behavior of bands sensitive to Trp β37. The emerging pattern is consistent with both a distribution of accessible T-state species and a tight coupling of proximal strain with the status of the hinge region of the T-state $\alpha_1\beta_2$ interface. These results closely match the recent conclusions of the Arnone group (*30*) based on a systematic X-ray crystallographic study of the progression of global and local changes seen within T-state crystals as a function of ligation for LT and HT species.

Distinct Functional T States Exposed Using MEM. The kinetically distinct populations derived from the MEM method of extracting kinetic lifetimes ($^1/_k$) for the bimolecular solvent phase under pseudo-first-order conditions (a large excess of CO relative to Hb) reveals multiple kinetic populations associated with ligated T-state species. These kinetic populations can be roughly grouped on the basis of the distribution of kinetic lifetimes ($^1/_k$) for the pseudo-first-order solvent phase CO recombination process. The same distinct populations are seen for different samples but with differing amplitudes. As shown in Table 2, these populations have been somewhat arbitrarily grouped into three low-affinity T populations (LT), one high-affinity T-state population (HT) and an R-state population. For each grouping, there is a bounded range of observed lifetime values. The preliminary results from new studies of how the MEM T-state populations evolve for [deoxyHbA] + CO indicate that with time, after the addition of CO, there is a progression within each T-state grouping from slower to faster rebinding times.

The distribution of the kinetic populations tracks with the photoproduct frequencies of ν(Fe−His). The samples with the lowest frequency for ν(Fe−His) yield kinetic populations heavily skewed toward the LTs with the longest lifetimes (slowest rebinding rates). There appears to be a clear progression, where the increase in frequency is associated with either the appearance of faster populations or the increase in the relative amplitude of the faster populations. The results suggest several trends. These include (i) for a given species, the addition of effectors usually shifts the distribution toward the slower LT population; (ii) for [deoxyHb] + CO samples, the encapsulation protocol allows for the manipulation of the distribution of LT and HT populations contributing to the kinetic traces at early times after the addition of CO; (iii) for a given T-state species, when comparing the populations of a T-state [COHb] sample with that of the corresponding [deoxyHb] + CO sample at early times, the populations associated with the former are biased toward HT and the faster LT populations; (iv) for a given set of solution or encapsulation conditions, the T-state sample with the lowest proximal strain and highest oxygen affinity will contain the highest fraction of the HT population; and (v) the progression from deoxy LT to ligated LT to ligated HT is correlated with a loosening of constraints associated with Trp β37 and Tyr α140.

Relating Conformation and Ligand Reactivity within the T Quaternary State. The present study shows that there are several functionally distinct conformations that can be accessed within the T quaternary state. This observation is consistent with several recent assessments of the allosteric mechanism within hemoglobin that postulate multiple tertiary states within either T or R (*12*, *15*, *98*, *103*, *104*). A challenge in observing and characterizing these multiple T-state conformations is that factors that favor the formation of the higher-affinity T-state conformations also favor the build up of the R-state population. In the present study, sol−gel encapsulation and mutagenesis allow for the build up of higher-affinity T-state conformations under conditions where, in solution with HbA, the population would be heavily biased toward the ligated R-state conformations.

Figure 9 depicts a hypothetical reaction-coordinate diagram that provides a framework for understanding the ligand-binding-induced changes within the T state. It is based on the present work, which clearly shows that there are distinct populations within the T-state family and that there is a clear progression of T-state populations in response to ligand binding. Furthermore, the slow, diffusive nature of the evolution of structure within the sol−gel is suggestive of a

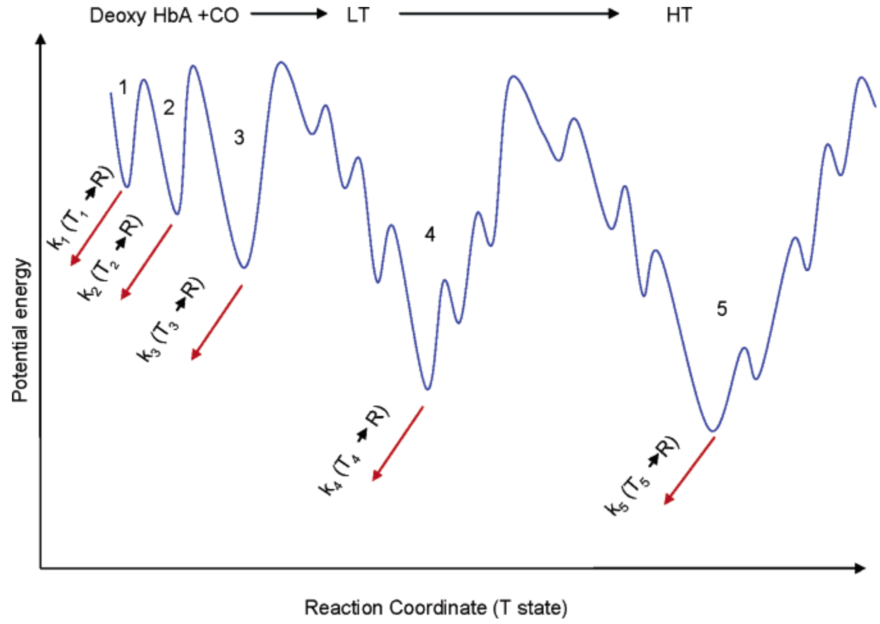

FIGURE 9: Hypothetical reaction-coordinate diagram depicting the proposed evolution of the T-state tertiary structure upon ligand binding. Perpendicular to this reaction coordinate is the reaction coordinate for the T → R transition. The numbered potential minima represent different T-state species that are progressively accessed after ligand binding. For HbA, the initial deoxy population is dominated by the potential well-labeled 1, which prior to ligand binding would be much deeper than that shown. The progression from 1 to 5 represents the T-state tetramer relaxation from the low-affinity T (LT) to high-affinity T (HT). In going from LT to HT (i.e., 1 → 5), the $\alpha_1\beta_2$ interface loosens, the proximal strain decreases, and the barrier for the T → R switch is reduced, resulting in a progressive increase in the T to R rate constant. Thus, for each T-state conformation (designated 1−5), there is a corresponding T to R rate constant $k_n(T_n \rightarrow R)$ with n being the designation for the specific T state. These rate constants increase as n goes from 1 to 5. Sol−gel encapsulation greatly slows $k(T \rightarrow R)$ relative to the LT → HT transition. The overall energy surface is portrayed as a rough energy landscape on the basis of the diffusive like evolution of conformation observed for the sol−gel samples.

rough energy surface as depicted in the Figure, which would be consistent with the proposed entropic search models (*105*, *106*) that account for protein conformational changes.

The present study reveals two reaction coordinates for conformational change that need to be considered for HbA-relaxation phenomena. One coordinate (the x axis) is for accessible conformations within the T state and thus describes the energy landscape that dictates the evolution of the T-state tertiary structure upon ligand binding. In addition, for each conformational substate or microstate within the T state, there is a perpendicular coordinate shown as a red arrow that describes the transition from the T to R state. Upon ligand binding to the hemes, the T-state population evolves from the now destabilized deoxy T-state end point (extreme left in Figure 9) toward the high-affinity T-state endpoint. The ligated T-state intermediates represent a loosened structure, suggestive of a transition state that provides a reduced-barrier pathway for accessing the R state. It follows that as the population evolves toward the high-affinity T-state intermediates, the barrier for the T to R state gets lower (and the rate $k(T \rightarrow R)$ gets faster). In solution, the rate at which the R state is accessed is sufficiently fast to preclude the buildup of measurable populations of the higher-affinity T-state species. Mutations such as Nβ102A and Wβ37E and sol−gel encapsulation can allow for the probing of the T-state conformational coordinate either by sufficiently destabilizing the R state relative to the T state or by slowing the T-to-R transition. It has been proposed that the stabilization of hydration shell waters of Hb by the sol−gel plays a role in raising the barrier for the T-to-R transition (*31*, *38*, *42*) because this transition is associated with a large increase in the degree of hydration of the tetramer (*107*−*112*).

The distribution of T-state conformations at any given time point after ligand binding appears to be the result of several competing forces acting on the tetramer. A framework for understanding these push−pull effects can be extracted from a model derived from several studies on the role of the segment of the hinge region of the $\alpha_1\beta_2$ interface that includes the Trp β37 cluster. Recent research has demonstrated that the major region of quaternary-T constraint is derived from the coupling between the conformational status of the Trp β37 cluster and the proximal strain at the α heme (*26*, *30*, *35*, *51*, *93*).

The present results imply that the stability of the Trp37 cluster also impacts the rate of conformational evolution. In sol−gel, the Hb(W(37E) mutant rapidly accesses HT upon ligand binding as do desArgHb and Hb(α140Y) mutants (unpublished observations). In contrast, similarly encapsulated deoxy derivatives of HbA and Hb(Nβ102A) in the presence of effectors, especially L35, exhibit a slow CO-induced evolution away from the low-affinity-end-point T-state conformation consistent with a stabilization of the β37 cluster.

Proposed Stereochemical Model: Quaternary State Modulation of Tertiary Conformations of the $\alpha\beta$ Dimers. The present results are consistent with effector-induced modulation of the tertiary structure impacting oxygen affinity (*12*, *104*), fitting of T-state kinetic data using a multi-tertiary structure model (*98*), and thermodynamic data indicating cooperativity within the T state (*20*, *21*, *113*). A promising new perspective that unifies these varied results and models is emerging from several lines of investigation. These include thermodynamic studies that indicate communication and a degree of cooperativity within $\alpha\beta$ dimers within the tetramer

(*20*, *21*, *114*, *115*), functional/spectroscopic studies (*116*) on isolated dimers (semi Hbs), and recent X-ray studies (*30*) that show that as the β37 cluster is loosened, there is a concomitant change in the bending of the individual $\alpha\beta$ dimers. The semi-Hb study (*116*) shows that ligand binding favors tertiary structures for the $\alpha\beta$ dimer that are either R-like or HT-like, whereas the absence of ligand and/or the addition of effectors favors the tertiary conformations that are more LT-like. However, in both cases, the dimer does not access the extremes in either the tertiary structure or the functionality associated with the tetramer. Thus, the conformational and functional parameters associated with both quaternary constraint and quaternary enhancements are not achieved for the isolated dimers, despite the large dynamic range of accessible conformations for isolated dimers.

The present study is consistent with a picture in which the degree to which the dimer within the T-state tetramer responds to ligation is governed by the stability of the Trp 37β cluster. When the β37 cluster/hinge is loosened, as occurs upon ligand binding within the T state, the dimer is no longer constrained and can now relax toward its preferred, that is, more stable conformation upon ligation even within the T quaternary state, as is also seen in the crystal study. The driving force for the switch to the ligated R structure now comes from the relative stabilities of the loosened T-state structure and the ligated R structure under conditions where the $\alpha\beta$ dimer is ligated.

CONCLUSIONS

The use of mutant forms of HbA and/or sol−gel encapsulation to slow or eliminate the ligand-binding-induced T → R transition has allowed for the spectroscopic and functional probing of different ligated T-state conformations. The results of the present study indicate that there is a distribution of functionally distinct ligated T conformations and that the conformational composition of observed composite populations is modulated by a number of factors that include the stability of the hinge region of the $\alpha_1\beta_2$ interface and the degree of ligation. The present results build on the earlier reports (*28*, *29*, *32*) on low- and high-affinity forms of the T state (LT and HT, respectively). The present study shows that upon full and partial ligand binding, solvent conditions, encapsulation in sol−gel matrices, and mutation influence the distribution of LT and HT populations. The data is consistent with ligand binding to deoxy Hb, initiating a progressive evolution both from LT to HT conformations and from slower to faster populations of LT and HT. There is associated with this progression, both a decrease in proximal strain/quaternary constraint and a weakening of the hinge interactions within the $\alpha_1\beta_2$ interface associated with the deoxy T state. The rate and extent of this relaxation appears to be a function of the stability of the so-called Trp β37 cluster of residues within the hinge region of the $\alpha_1\beta_2$ interface as well as the presence or the absence of allosteric effectors. The results are consistent with a picture in which the T-quaternary state encompasses a range of accessible $\alpha\beta$-dimer conformations and the distribution of dimer conformations observed for a given T-state population is a function of the ligation and effector-dependent stability of the Trp β37 cluster of residues. The results can also account for the large range of T-state oxygen affinities associated with HbA in terms of the environment-/effector-dependent extent to which the T-state tertiary structure evolves after oxygen binding. The evolved, ligated T-state distribution of the conformational states will determine the off rate of the bound oxygens, which is the major determinant of oxygen-binding affinity.

ACKNOWLEDGMENT

The mutant hemoglobins were the generous gift of Professor R. Noble. We thank Professor Robert Noble, Laura Kwiatkowski, and Hilda Hui for there careful reading of the manuscript and their helpful suggestions and insights.

REFERENCES

1. Monod, J., Wyman, J., and Changeux, J. P. (1965) On the nature of allosteric transitions: a plausible model, *J. Mol. Biol. 12*, 88−118.
2. Eaton, W. A., Henry, E. R., Hofrichter, J., and Mozzarelli, A. (1999) Is cooperative oxygen binding by hemoglobin really understood?, *Nat. Struct. Biol. 6*, 351−358.
3. Perutz, M. F., Fermi, G., Luisi, B., Shaanan, B., and Liddington, R. C. (1987) Stereochemistry of cooperative mechanisms in hemoglobin, *Cold Spring Harbor Symp. Quant. Biol. 52*, 555−565.
4. Perutz, M. F., Wilkinson, A. J., Paoli, M., and Dodson, G. G. (1998) The stereochemical mechanism of the cooperative effects in hemoglobin revisited, *Annu. Rev. Biophys. Biomol. Struct. 27*, 1−34.
5. Shulman, R. G., Ogawa, S., and Hopfield, J. J. (1972) An allosteric model of hemoglobin, *Cold Spring Harbor Symp. Quant. Biol. 36*, 337−341.
6. Shulman, R. G. (2001) Spectroscopic contributions to the understanding of hemoglobin function: implications for structural biology, *IUBMB Life 51*, 351−357.
7. Mueser, T. C., Rogers, P. H., and Arnone, A. (2000) Interface sliding as illustrated by the multiple quaternary structures of liganded hemoglobin, *Biochemistry 39*, 15353−15364.
8. Lukin, J. A., Kontaxis, G., Simplaceanu, V., Yuan, Y., Bax, A., and Ho, C. (2003) Quaternary structure of hemoglobin in solution, *Proc. Natl. Acad. Sci. U.S.A. 100*, 517−520.
9. Fermi, G., Perutz, M. F., Shaanan, B., and Fourme, R. (1984) The crystal structure of human deoxyhaemoglobin at 1.74 A resolution, *J. Mol. Biol. 175*, 159−174.
10. Kavanaugh, J. S., Rogers, P. H., Case, D. A., and Arnone, A. (1992) High-resolution X-ray study of deoxyhemoglobin Rothschild 37 beta Trp → Arg: a mutation that creates an intersubunit chloride-binding site, *Biochemistry 31*, 4111−4121.
11. Kavanaugh, J. S., Chafin, D. R., Arnone, A., Mozzarelli, A., Rivetti, C., Rossi, G. L., Kwiatkowski, L. D., and Noble, R. W. (1995) Structure and oxygen affinity of crystalline desArg141 alpha human hemoglobin A in the T state, *J. Mol. Biol. 248*, 136−150.
12. Tsuneshige, A., Park, S., and Yonetani, T. (2002) Heterotropic effectors control the hemoglobin function by interacting with its T and R states—a new view on the principle of allostery, *Biophys. Chem. 98*, 49−63.
13. Yonetani, T., Park, S. I., Tsuneshige, A., Imai, K., and Kanaori, K. (2002) Global allostery model of hemoglobin. Modulation of O(2) affinity, cooperativity, and Bohr effect by heterotropic allosteric effectors, *J. Biol. Chem. 277*, 34508−34520.
14. Bonaventura, C., Tesh, S., Faulkner, K. M., Kraiter, D., and Crumbliss, A. L. (1998) Conformational fluctuations in deoxy hemoglobin revealed as a major contributor to anionic modulation of function through studies of the oxygenation and oxidation of hemoglobins A0 and Deer Lodge beta2(NA2)His → *Arg, Biochemistry 37*, 496−506.
15. Imai, K., Tsuneshige, A., and Yonetani, T. (2002) Description of hemoglobin oxygenation under universal solution conditions by a global allostery model with a single adjustable parameter, *Biophys. Chem. 98*, 79−91.
16. Tsuneshige, A., Zhou, Y. X., and Yonetani, T. (1993) Oxygen equilibrium studies of cross-linked iron-cobalt hybrid hemoglobins. Models for partially ligated intermediates of cobalt hemoglobin, *J. Biol. Chem. 268*, 23031−23040.

17. Shibayama, N., Yonetani, T., Regan, R. M., and Gibson, Q. H. (1995) Mechanism of ligand binding to Ni(II)-Fe(II) hybrid hemoglobins, *Biochemistry 34*, 14658−14667.
18. Fujii, M., Hori, H., Miyazaki, G., Morimoto, H., and Yonetani, T. (1993) The porphyrin-iron hybrid hemoglobins. Absence of the Fe−His bonds in one type of subunits favors a deoxy-like structure with low oxygen affinity, *J. Biol. Chem. 268*, 15386-15393.
19. Miyazaki, G., Morimoto, H., Yun, K. M., Park, S. Y., Nakagawa, A., Minagawa, H., and Shibayama, N. (1999) Magnesium(II) and zinc(II)-protoporphyrin IX's stabilize the lowest oxygen affinity state of human hemoglobin even more strongly than deoxyheme, *J. Mol. Biol. 292*, 1121−1136.
20. Ackers, G. K., Holt, J. M., Huang, Y., Grinkova, Y., Klinger, A. L., and Denisov, I. (2000) Confirmation of a unique intra-dimer cooperativity in the human hemoglobin alpha(1)beta(1)half-oxygenated intermediate supports the symmetry rule model of allosteric regulation, *Proteins Suppl*. 23−43.
21. Ackers, G. K., Holt, J. M., Burgie, E. S., and Yarian, C. S. (2004) Analyzing intermediate state cooperativity in hemoglobin, *Methods Enzymol. 379*, 3−28.
22. Shibayama, N., Morimoto, H., and Kitagawa, T. (1986) Properties of chemically modified Ni(II)-Fe(II) hybrid hemoglobins. Ni(II) protoporphyrin IX as a model for a permanent deoxy-heme, *J. Mol. Biol. 192*, 331−336.
23. Unzai, S., Hori, H., Miyazaki, G., Shibayama, N., and Morimoto, H. (1996) Oxygen equilibrium properties of chromium (III)-iron (II) hybrid hemoglobins, *J. Biol. Chem. 271*, 12451−12456.
24. Kiger, L., Klinger, A. L., Kwiatkowski, L. D., De Young, A., Doyle, M. L., Holt, J. M., Noble, R. W., and Ackers, G. K. (1998) Thermodynamic studies on the equilibrium properties of a series of recombinant betaW37 hemoglobin mutants, *Biochemistry 37*, 4336−4345.
25. Kwiatkowski, L. D., Hui, H. L., Wierzba, A., Noble, R. W., Walder, R. Y., Peterson, E. S., Sligar, S. G., and Sanders, K. E. (1998) Preparation and kinetic characterization of a series of betaW37 variants of human hemoglobin A: evidence for high-affinity T quaternary structures, *Biochemistry 37*, 4325−4335.
26. Noble, R. W., Hui, H. L., Kwiatkowski, L. D., Paily, P., DeYoung, A., Wierzba, A., Colby, J. E., Bruno, S., and Mozzarelli, A. (2001) Mutational effects at the subunit interfaces of human hemoglobin: evidence for a unique sensitivity of the T quaternary state to changes in the hinge region of the alpha 1 beta 2 interface, *Biochemistry 40*, 12357−12368.
27. Goldbeck, R. A., Esquerra, R. M., Holt, J. M., Ackers, G. K., and Kliger, D. S. (2004) The molecular code for hemoglobin allostery revealed by linking the thermodynamics and kinetics of quaternary structural change. 1. microstate linear free energy relations, *Biochemistry 43*, 12048−12064.
28. Bruno, S., Bonaccio, M., Bettati, S., Rivetti, C., Viappiani, C., Abbruzzetti, S., and Mozzarelli, A. (2001) High and low oxygen affinity conformations of T state hemoglobin, *Protein Sci. 10*, 2401−2407.
29. Shibayama, N., and Saigo, S. (2001) Direct observation of two distinct affinity conformations in the T state human deoxyhemoglobin, *FEBS Lett. 492*, 50−53.
30. Kavanaugh, J. S., Rogers, P. H., and Arnone, A. (2005) Crystallographic Evidence for a new ensemble of ligand-induced allosteric transitions in hemoglobin: the T-to-T(High) quaternary transitions, *Biochemistry 44*, 6101−6121.
31. Samuni, U., Juszczak, L., Dantsker, D., Khan, I., Friedman, A. J., Perez-Gonzalez-de-Apodaca, J., Bruno, S., Hui, H. L., Colby, J. E., Karasik, E., Kwiatkowski, L. D., Mozzarelli, A., Noble, R., and Friedman, J. M. (2003) Functional and spectroscopic characterization of half-liganded iron−zinc hybrid hemoglobin: evidence for conformational plasticity within the T state, *Biochemistry 42*, 8272−8288.
32. Samuni, U., Dantsker, D., Juszczak, L. J., Bettati, S., Ronda, L., Mozzarelli, A., and Friedman, J. M. (2004) Spectroscopic and functional characterization of T state hemoglobin conformations encapsulated in silica gels, *Biochemistry 43*, 13674−13682.
33. Yanase, H., Manning, L. R., Vandegriff, K., Winslow, R. M., and Manning, J. M. (1995) A recombinant human hemoglobin with asparagine-102(beta) substituted by alanine has a limiting low oxygen affinity, reduced marginally by chloride, *Protein Sci. 4*, 21−28.
34. Hui, H. L., Kwiatkowski, L. D., Karasik, E., Colby, J. E., and Noble, R. W. (2004) Ligand binding to symmetrical FeZn hybrids of variants of human HbA with modifications in the alpha1-beta2 interface, *Biochemistry 43*, 7843−7850.
35. Kavanaugh, J. S., Weydert, J. A., Rogers, P. H., and Arnone, A. (1998) High-resolution crystal structures of human hemoglobin with mutations at tryptophan 37beta: structural basis for a high-affinity T state, *Biochemistry 37*, 4358−4373.
36. Peterson, E. S., and Friedman, J. M. (1998) A possible allosteric communication pathway identified through a resonance Raman study of four β37 mutants of human hemoglobin A, *Biochemistry 37*, 4346−4357.
37. Bettati, S., and Mozzarelli, A. (1997) T state hemoglobin binds oxygen noncooperatively with allosteric effects of protons, inositol hexaphosphate, and chloride, *J. Biol. Chem. 272*, 32050−32055.
38. Khan, I., Shannon, C. F., Dantsker, D., Friedman, A. J., Perez-Gonzalez-de-Apodaca, J., and Friedman, J. M. (2000) Sol−gel trapping of functional intermediates of hemoglobin: geminate and bimolecular recombination studies, *Biochemistry 39*, 16099−16109.
39. Samuni, U., Dantsker, D., Khan, I., Friedman, A. J., Peterson, E., and Friedman, J. M. (2002) Spectroscopically and kinetically distinct conformational populations of sol-gel-encapsulated carbonmonoxy myoglobin. A comparison with hemoglobin, *J. Biol. Chem. 277*, 25783−25790.
40. Shibayama, N., and Saigo, S. (1995) Fixation of the quaternary structures of human adult haemoglobin by encapsulation in transparent porous silica gels, *J. Mol. Biol. 251*, 203−209.
41. Das, T. K., Khan, I., Rousseau, D. L., and Friedman, J. M. (1999) Temperature-dependent quaternary state relaxation in sol-gel encapsulated hemoglobin, *Biospectroscopy 5(S)*, 64−70.
42. Samuni, U., Dantsker, D., Khan, I., Friedman, A. J., Peterson, E., and Friedman, J. M. (2002) Spectroscopically and kinetically distinct conformational populations of sol-gel encapsulated carbonmonoxy myoglobin: a comparison with hemoglobin, *J. Biol. Chem. 277*, 25783−25790.
43. Friedman, J. M. (1985) Structure, dynamics, and reactivity in hemoglobin, *Science 228*, 1273−1280.
44. Friedman, J. M. (1994) Time-resolved resonance Raman spectroscopy as probe of structure, dynamics, and reactivity in hemoglobin, *Methods Enzymol. 232*, 205−231.
45. Rousseau, D. L., and Friedman, J. M. (1988) in *Biological Applications of Raman Spectroscopy* (Spiro, T. G., Ed.) pp 133−215, John Wiley & Sons, New York.
46. Friedman, J. M., Scott, T. W., Stepnoski, R. A., Ikeda-Saito, M., and Yonetani, T. (1983) The iron-proximal histidine linkage and protein control of oxygen binding in hemoglobin. A transient Raman study, *J. Biol. Chem. 258*, 10564−10572.
47. Hu, X., Rodgers, K. R., Mukerji, I., and Spiro, T. G. (1999) New light on allostery: dynamic resonance Raman spectroscopy of hemoglobin kempsey, *Biochemistry 38*, 3462−3467.
48. Bangcharoenpaurpong, O., Schomaker, K. T., and Champion, P. M. (1984) A resonance Raman investigation of myoglobin and hemoglobin, *J. Am. Chem. Soc. 106*, 5688−5698.
49. Champion, P. M. (1992) Raman and kinetic studies of myoglobin structure and dynamics, *J. Raman. Spectrosc. 23*, 557−567.
50. Kitagawa, T. (1988) in *Biological Application of Raman Spectroscopy* (Spiro, T. G., Ed.) pp 97−131, John Wiley & Sons, New York.
51. Peterson, E. S., and Friedman, J. M. (1998) A possible allosteric communication pathway identified through a resonance Raman study of four beta37 mutants of human hemoglobin A, *Biochemistry 37*, 4346−4357.
52. Peterson, E. S., Shinder, R., Khan, I., Juczszak, L., Wang, J., Manjula, B., Acharya, S. A., Bonaventura, C., and Friedman, J. M. (2004) Domain-specific effector interactions within the central cavity of human adult hemoglobin in solution and in porous sol−gel matrixes: evidence for long-range communication pathways, *Biochemistry 43*, 4832−4843.
53. Austin, J. C., Rodgers, K. R., and Spiro, T. G. (1993) Protein structure from ultraviolet resonance Raman spectroscopy, *Methods Enzymol. 226*, 374−396.
54. Asher, S. (1993) UV resonance Raman spectroscopy for analytical, physical and biophysical chemistry. Part 1, *Anal. Chem. 65*, 59A−66A.
55. Austin, J., Jordan, T., and Spiro, T. (1993) in *Biomolecular Spectroscopy Part A* (Clark, R. J. H., and Hester, R. E., Eds.) pp 55−127, John Wiley & Sons, New York.
56. Kitagawa, T. (1992) Investigation of the higher order structure of proteins by ultraviolet resonance Raman spectroscopy, *Prog. Biophys. Mol. Biol. 58*, 1−18.

57. Huang, S., Peterson, E. S., Ho, C., and Friedman, J. M. (1997) Quaternary structure sensitive tyrosine interactions in hemoglobin: a UV resonance Raman study of the double mutant rHb (beta99Asp→Asn, alpha42Tyr→Asp), *Biochemistry 36*, 6197−6206.
58. Huang, J., Juszczak, L. J., Peterson, E. S., Shannon, C. F., Yang, M., Huang, S., Vidugiris, G. V., and Friedman, J. M. (1999) The conformational and dynamic basis for ligand binding reactivity in hemoglobin Ypsilanti (beta 99 asp→Tyr): origin of the quaternary enhancement effect, *Biochemistry 38*, 4514−4525.
59. Juszczak, L. J., and Friedman, J. M. (1999) UV resonance Raman spectra of ligand binding intermediates of sol-gel encapsulated hemoglobin, *J. Biol. Chem. 274*, 30357−30360.
60. Juszczak, L. J., Fablet, C., Baudin-Creuza, V., Lesecq-Le Gall, S., Hirsch, R. E., Nagel, R. L., Friedman, J. M., and Pagnier, J. (2003) Conformational changes in hemoglobin S (betaE6V) imposed by mutation of the beta Glu7-beta Lys132 salt bridge and detected by UV resonance Raman spectroscopy, *J. Biol. Chem. 278*, 7257−7263.
61. Rodgers, K. R., and Spiro, T. G. (1994) Nanosecond dynamics of the R→T transition in hemoglobin: ultraviolet Raman studies, *Science 265*, 1697−1699.
62. Zhao, X., Chen, R., Raj, V., and Spiro, T. G. (2001) Assignment of the 1511 cm^{-1} UV resonance Raman marker band of hemoglobin to tryptophan, *Biopolymers 62*, 158−162.
63. Balakrishnan, G., Case, M. A., Pevsner, A., Zhao, X., Tengroth, C., McLendon, G. L., and Spiro, T. G. (2004) Time-resolved absorption and UV resonance Raman spectra reveal stepwise formation of T quaternary contacts in the allosteric pathway of hemoglobin, *J. Mol. Biol. 340*, 843−856.
64. Wang, D., and Spiro, T. G. (1998) Structure changes in hemoglobin upon deletion of *C*-terminal residues, monitored by resonance Raman spectroscopy, *Biochemistry 37*, 9940−9951.
65. Wang, D., Zhao, X., Shen, T.-J., Ho, C., and Spiro, T. (1999) Role of interhelical H-bonds [Wα14-Tα67 and Wβ15-Sβ72] in the hemoglobin allosteric reaction path evaluated by UV resonance Raman spectroscopy of site-mutants, *J. Am. Chem. Soc. 121*, 11197−11203.
66. Jayaraman, V., and Spiro, T. G. (1995) Structure of a third cooperativity state of hemoglobin: ultraviolet resonance Raman spectroscopy of cyanomethemoglobin ligation microstates, *Biochemistry 34*, 4511−4515.
67. Jayaraman, V., Rodgers, K. R., Mukerji, I., and Spiro, T. G. (1993) R and T states of fluoromethemoglobin probed by ultraviolet resonance Raman spectroscopy, *Biochemistry 32*, 4547−4551.
68. Alpert, B., El Mohsni, S., Lindqvist, L., Tfibel, F. (1979) Transient effects in the nanosecond laser photolysis of carbonmonoxyhemoglobin: Cage recombination and spectral evolution of the protein, *Chem. Phys. Lett. 64*, 11−16.
69. Duddell, D., Morris, R., and Richards, J. (1979) Ultrafast recombination in nanosecond laser photolysis of carbonylhemoglobin, *J. Chem. Soc., Chem. Commun. 2*, 75−76.
70. Duddell, D. A., Morris, R. J., Muttucumaru, N. J., and Richards, J. T. (1980) The dependence of the quantum yield of ligand photodissociation from haem proteins on ultrafast recombination, *Photochem. Photobiol. 11*, 479−484.
71. Friedman, J. M., and Lyons, K. B. (1980) Transient Raman study of CO-haemoprotein photolysis: origin of the quantum yield, *Nature 284*, 570−572.
72. Lalezari, I., Lalezari, P., Poyart, C., Marden, M., Kister, J., Bohn, B., Fermi, G., and Perutz, M. F. (1990) New effectors of human hemoglobin: structure and function, *Biochemistry 29*, 1515−23.
73. Doyle, M. L., Lew, G., De Young, A., Kwiatkowski, L., Wierzba, A., Noble, R. W., and Ackers, G. K. (1992) Functional properties of human hemoglobins synthesized from recombinant mutant beta-globins, *Biochemistry 31*, 8629−8639.
74. Chatterjee, R., Welty, E. V., Walder, R. Y., Pruitt, S. L., Rogers, P. H., Arnone, A., and Walder, J. A. (1986) Isolation and characterization of a new hemoglobin derivative cross-linked between the alpha chains (lysine 99 alpha 1—lysine 99 alpha 2), *J. Biol. Chem. 261*, 9929−9937.
75. Snyder, S. R., Welty, E. V., Walder, R. Y., Williams, L. A., and Walder, J. A. (1987) HbXL99 alpha: a hemoglobin derivative that is cross-linked between the alpha subunits is useful as a blood substitute, *Proc. Natl. Acad. Sci. U.S.A. 84*, 7280−7284.
76. Snyder, S. R., and Walder, J. A. (1991) Chemically modified and recombinant hemoglobin blood substitutes, *Biotechnology 19*, 101−116.
77. Samuni, U., Navati, M. S., Juszczak, L. J., Dantsker, D., Yang, M., and Friedman, J. M. (2000) Unfolding and refolding of sol−gel encapsulated carbonmonoxymyoglobin: An orchestrated spectroscopic study of intermediates and kinetics, *J. Phys. Chem. B 104*, 10802−10813.
78. Juszczak, L. J., Manjula, B., Bonaventura, C., Acharya, S. A., and Friedman, J. M. (2002) UV resonance Raman study of beta93-modified hemoglobin A: chemical modifier-specific effects and added influences of attached poly(ethylene glycol) chains, *Biochemistry 41*, 376−385.
79. Samuni, U., Dantsker, D., Ray, A., Wittenberg, J. B., Wittenberg, B. A., Dewilde, S., Moens, L., Ouellet, Y., Guertin, M., and Friedman, J. M. (2003) Kinetic modulation in carbonmonoxy derivatives of truncated hemoglobins: The role of distal heme pocket residues and extended apolar tunnel, *J. Biol. Chem. 278*, 27241−27250.
80. Dantsker, D., Samuni, U., Friedman, A. J., Yang, M., Ray, A., and Friedman, J. M. (2002) Geminate rebinding in trehalose-glass embedded myoglobins reveals residue-specific control of intramolecular trajectories, *J. Mol. Biol. 315*, 239−251.
81. Kumar, A. T. N., Zhu, L., Christian, J. F., Demidov, A. A., and Champion, P. M. (2001) On the rate distribution analysis of kinetic data using the maximum entropy method: applications to myoglobin relaxation on the nanosecond and femtosecond time scales, *J. Phys. Chem. B 105*, 7847−7856.
82. Lavalette, D., Tetreau, C., Brochon, J. C., and Livesey, A. (1991) Conformational fluctuations and protein reactivity. Determination of the rate-constant spectrum and consequences in elementary biochemical processes, *Eur. J. Biochem. 196*, 591−598.
83. Steinbach, P. J., Chu, K., Frauenfelder, H., Johnson, J. B., Lamb, D. C., Nienhaus, G. U., Sauke, T. B., and Young, R. D. (1992) Determination of rate distributions from kinetic experiments, *Biophys. J. 61*, 235−245.
84. Steinbach, P. J. (1996)Two-dimensional distributions of activation enthalpy and entropy from kinetics by the maximum entropy method *Biophys. J. 70*, 1521−8.
85. Tetreau, C., Tourbez, M., Gorren, A., Mayer, B., and Lavalette, D. (1999) Dynamics of carbon monoxide binding with neuronal nitric oxide synthase, *Biochemistry 38*, 7210−7218.
86. Dantsker, D., Roche, C., Samuni, U., Blouin, G., Olson, J. S., and Friedman, J. M. (2005) The position 68(E11) side chain in myoglobin regulates ligand capture, bond formation with heme iron, and internal movement into the Xe cavities, *J. Biol. Chem. 280*, 38740−38755.
87. Siemiarczuk, A., and Ware, W. R. (1989) Temperature dependence of fluorescence lifetime distributions in 1,3-di(1-pyrenyl)propane with maximum entropy method, *J. Phys. Chem. 93*, 7609−7618.
88. Siemiarczuk, A., Wagner, B. D., and Ware, W. R. (1990) Comparison of the maximum entropy and exponential series methods for the recovery of distributions of lifetimes from fluorescence lifetime data, *J. Phys. Chem. 94*, 1661−1666.
89. Podstawka, E., Rajani, C., Kincaid, J. R., and Proniewicz, L. M. (2000) Resonance Raman studies of heme structural differences in subunits of deoxy hemoglobin, *Biopolymers 57*, 201−207.
90. Su, C., Park, Y. D., Liu, G., and Spiro, T. G. (1989) Hemoglobin quaternary structure change monitored directly by transient UV resonance Raman spectroscopy, *J. Am. Chem. Soc. 111*, 3457−3459.
91. Rodgers, K., Su, S., Subramaniam, S., and Spiro, T. (1992) Hemoglobin R→T structural dynamics from simultaneous monitoring of tyrosine and tryptophan time-resolved UV resonance Raman signals *J. Am. Chem. Soc. 114*, 3697−3709.
92. Jayaraman, V., Rodgers, K. R., Mukerji, I., and Spiro, T. G. (1995) Hemoglobin allostery: resonance Raman spectroscopy of kinetic intermediates, *Science 269*, 1843−1848.
93. Juszczak, L., Samuni, U., and Friedman, J. M. (2005) Conformational and functional significance of the alpha140 side-chain in HbA: a UV and visible resonance Raman study of three alpha140 mutants, *J. Raman Spectrosc. 36*, 350−358.
94. Antonini, E., and Brunori, M. (1971) *Hemoglobins and Myoglobins in their Reactions with Ligands*, North-Holland Publishing Co., Amsterdam, The Netherlands.
95. Hofrichter, J., Henry, E. R., Sommer, J. H., Deutsch, R., Ikeda-Saito, M., Yonetani, T., and Eaton, W. A. (1985) Nanosecond optical spectra of iron−cobalt hybrid hemoglobins: geminate recombination, conformational changes, and intersubunit communication, *Biochemistry 24*, 2667−2679.
96. Dantsker, D., Samuni, U., Friedman, J. M., and Agmon, N. (2005) A hierarchy of functionally important relaxations within myoglobin

based on solvent effects, mutations and kinetic model, *Biochim. Biophys. Acta 1749*, 234−251.

97. Khan, I., Dantsker, D., Samuni, U., Friedman, A. J., Bonaventura, C., Manjula, B., Acharya, S. A., and Friedman, J. M. (2001) Beta 93 modified hemoglobin: kinetic and conformational consequences, *Biochemistry 40*, 7581−7592.
98. Viappiani, C., Bettati, S., Bruno, S., Ronda, L., Abbruzzetti, S., Mozzarelli, A., and Eaton, W. A. (2004) New insights into allosteric mechanisms from trapping unstable protein conformations in silica gels, *Proc. Natl. Acad. Sci. U.S.A. 101*, 14414−14419.
99. Scott, T. W., and Friedman, J. M. (1984) Tertiary-structure relaxation in hemoglobin: a transient Raman study, *J. Am. Chem. Soc. 106*, 5677−5687.
100. Wajcman, H., Kister, J., Galacteros, F., Spielvogel, A., Lin, M. J., Vidugiris, G. J., Hirsch, R. E., Friedman, J. M., and Nagel, R. L. (1996) Hb Montefiore (126(H9)Asp→Tyr). High oxygen affinity and loss of cooperativity secondary to C-terminal disruption, *J. Biol. Chem. 271*, 22990−22998.
101. Ondrias, M. R., Rousseau, D. L., Shelnutt, J. A., and Simon, S. R. (1982) Quaternary-transformation-induced changes at the heme in deoxyhemoglobins, *Biochemistry 21*, 3428−3437.
102. Friedman, J. M., Rousseau, D. L., Ondrias, M. R., and Stepnoski, R. A. (1982) Transient Raman study of hemoglobin: structural dependence of the iron- histidine linkage, *Science 218*, 1244−1246.
103. Henry, E. R., Bettati, S., Hofrichter, J., and Eaton, W. A. (2002) A tertiary two-state allosteric model for hemoglobin, *Biophys. Chem. 98*, 149−164.
104. Yonetani, T., Park, S., Tsuneshige, A., Imai, K., and Kanaori, K. (2002) Global allostery model of hemoglobin: Modulation of O2-affinity, cooperativity, and Bohr effect by heterotropic allosteric effectors, *J. Biol. Chem. 277*, 34508−34520.
105. Fenimore, P. W., Frauenfelder, H., McMahon, B. H., and Young, R. D. (2004) Bulk-solvent and hydration-shell fluctuations, similar to alpha- and beta-fluctuations in glasses, control protein motions and functions, *Proc. Natl. Acad. Sci. U.S.A. 101*, 14408−14413.
106. Frauenfelder, H., Fenimore, P. W., and McMahon, B. H. (2002) Hydration, slaving and protein function, *Biophys. Chem. 98*, 35−48.
107. Colombo, M. F., and Sanches, R. (1990) Hydration-dependent conformational states of hemoglobin. Equilibrium and kinetic behavior, *Biophys. Chem. 36*, 33−39.
108. Colombo, M. F., Rau, D. C., and Parsegian, V. A. (1992) Protein solvation in allosteric regulation: a water effect on hemoglobin, *Science 256*, 655−659.
109. Colombo, M. F., and Bonilla-Rodriguez, G. O. (1996) The water effect on allosteric regulation of hemoglobin probed in water/glucose and water/glycine solutions, *J. Biol. Chem. 271*, 4895−4899.
110. Parsegian, V. A., Rand, R. P., Fuller, N. L., and Rau, D. C. (1986) Osmotic stress for the direct measurement of intermolecular forces, *Methods Enzymol. 127*, 400−416.
111. Parsegian, V. A., Rand, R. P., and Rau, D. C. (1995) Macromolecules and water: probing with osmotic stress, *Methods Enzymol. 259*, 43−94.
112. Colombo, M. F., and Seixas, F. A. (1999) Novel allosteric conformation of human HB revealed by the hydration and anion effects on O(2) binding, *Biochemistry 38*, 11741−11748.
113. Ackers, G. K., Dalessio, P. M., Lew, G. H., Daugherty, M. A., and Holt, J. M. (2002) Single residue modification of only one dimer within the hemoglobin tetramer reveals autonomous dimer function, *Proc. Natl. Acad. Sci. U.S.A. 99*, 9777−9782.
114. Hui, H. L., Kavanaugh, J. S., Doyle, M. L., Wierzba, A., Rogers, P. H., Arnone, A., Holt, J. M., Ackers, G. K., and Noble, R. W. (1999) Structural and functional properties of human hemoglobins reassembled after synthesis in *Escherichia coli*, *Biochemistry 38*, 1040−1049.
115. Goldbeck, R. A., Esquerra, R. M., Kliger, D. S., Holt, J. M., and Ackers, G. K. (2004) The molecular code for hemoglobin allostery revealed by linking the thermodynamics and kinetics of quaternary structural change. 2. Cooperative free energies of (alpha(FeCO)-beta(Fe))(2) and (alpha(Fe)beta(FeCO))(2) T state tetramers, *Biochemistry 43*, 12065−12080.
116. Tsuneshige, A., Kanaori, K., Samuni, U., Danstker, D., Friedman, J. M., Neya, S., Giangiacomo, L., and Yonetani, T. (2004) Semihemoglobins: High oxygen affinity dimeric forms of human hemoglobin respond efficiently to allosteric effectors without forming tetramers, *J. Biol. Chem. 279*, 48959−48967.

BI050010I